Monthly Notices
of the
ROYAL ASTRONOMICAL SOCIETY

MNRAS **513,** 4278–4294 (2022)
Advance Access publication 2022 April 29

https://doi.org/10.1093/mnras/stac1173

The magnetic fields of β Coronae Borealis and the early F-star σ Bootis

J. M. Seach [1]★ S. C. Marsden [1] B. D. Carter [1] C. Neiner [2] and C. P. Folsom [3]

[1] *Centre for Astrophysics, University of Southern Queensland, Toowoomba 4350, Australia*
[2] *LESIA, Paris Observatory, PSL University, CNRS, Sorbonne University, Université de Paris, 5 place Jules Janssen, F-92195 Meudon, France*
[3] *Tartu Observatory, University of Tartu, Observatooriumi 1, Tõravere 61602, Estonia*

Accepted 2022 April 25. Received 2022 April 25; in original form 2022 February 25

ABSTRACT

The study of magnetism in stars close to the transition from fossil to dynamo magnetic fields is important for understanding the nature of the stellar dynamo and dynamics of the outer atmosphere. We present surface magnetic maps for two stars that are located on opposite sides of the suspected transition zone: the chemically peculiar late A-star β Coronae Borealis (A9SrEuCr) and the early F-star σ Bootis (F3V). The large-scale magnetic field reconstructed at six epochs for β Coronae Borealis shows a complex fossil magnetic field, which is highly poloidal, and contains almost half the magnetic energy in higher multipoles ($\ell > 1$). In contrast, the single epoch magnetic map for σ Bootis contains a simple surface magnetic topology that is mostly poloidal, and predominantly dipolar, and is consistent with observations of other mature late F-stars.

Key words: stars: activity – stars: early-type – stars: magnetic field – stars: solar-type.

1 INTRODUCTION

We present the third paper in our series on magnetic fields in F-type stars. In the first paper, we published a magnetic snapshot survey of F-type stars (Seach et al. 2020, hereafter Paper 1), and in the second paper we reconstructed surface magnetic maps and created wind models for two late F-type stars β Vir (F9V) and θ Dra (F8IV) (Seach et al. 2022, hereafter Paper 2). In this paper, we present surface magnetic maps for the chemically peculiar star β Coronae Borealis (β CrB) and the F3V star σ Bootis (σ Boo). β CrB is a chemically peculiar star, classified as A9SrEuCr by Renson & Manfroid (2009), which is located on the hot side of the transition between fossil and dynamo magnetic fields. F-type stars are important targets for stellar magnetic studies since they span a range of masses where the transition from fossil to dynamo magnetic fields is believed to occur (Schatzman 1962; Mullan 1972; Schmitt et al. 1985; Wolff, Boesgaard & Simon 1986; Walter & Schrijver 1987; Seach et al. 2022).

Fossil fields (Cowling 1945; Spitzer 1958; Mestel 1967; Dudorov & Khaibrakhmanov 2015) are found in hot stars with little or no outer convection zone. The fields are thought to be left over from the star's formation where it undergoes gravitational collapse from a molecular cloud (Mestel & Spitzer 1956; Mestel 1966), from stellar mergers (Schneider et al. 2019), or from pre-main-sequence dynamos (Moss 2001). Fossil fields are frozen (Cowling 1957; Alfven, Alfvén & Fälthammar 1963) into the stellar atmosphere and essentially remain unchanged over the lifetime of the star. Classically, fossil fields have strengths ranging from a few hundred gauss up to 34 kG (Babcock 1960) and have been found in about 10 per cent of hot stars (Fossati et al. 2015; Grunhut et al. 2016; Sikora et al. 2019). More recently, another class of magnetic fields have been discovered in Ap and Fp stars with sub-gauss magnetic strengths and are possibly fossil in origin (Lignières et al. 2009; Petit et al. 2010; Neiner, Wade & Sikora 2017). Like the stronger fossil fields, these ultra-weak fields are possibly unchanged over long periods of time (Neiner et al. 2017).

Dynamo magnetic fields are located in the outer convection zone of cool stars where they are most efficiently generated by the action of turbulent convection and stellar rotation (Parker 1955, 1987). The presence of a deepening outer convection zone around early to mid-F-stars corresponds to the onset of dynamo-generated magnetic fields. There is an extensive literature on dynamo magnetic fields; e.g. see reviews by Moffatt (1978), Parker (1979), Krause & Radler (1980), Zeldovich, Ruzmaikin & Sokolov (1983), Roberts (1992), Brandenburg & Subramanian (2005), Mestel (2012), and Moffatt & Dormy (2019). Dynamo-generated magnetic fields are seen on the Sun and other solar-type stars where they are responsible for magnetic features like cool surface spots (Berdyugina 2005; Strassmeier 2009), flares (Pettersen 1989), stellar winds, and space weather phenomenon (Bothmer & Daglis 2007; Hanslmeier 2007; Singh et al. 2021). Increasing interest is developing in the field of exoplanet research (Perryman 2018) where the host star magnetic field has an important influence in the exoplanetary environment (Lammer & Khodachenko 2014; Linsky 2019). Dynamo magnetic fields are distinguished from fossil fields by their dynamic and changing nature with short decay times (Pevtsov, Canfield & Metcalf 1994; Burnette, Canfield & Pevtsov 2004).

β CrB is a well-known magnetic star (Babcock 1949, 1958; Stibbs 1950; Preston & Sturch 1967; Wolff & Wolff 1970) with a fossil field that has not been previously mapped using Zeeman Doppler imaging (ZDI). The star is suitable for magnetic studies due to its brightness and sharp spectral lines (Glagolevskij & Gerth 2003). Wolff & Wolff (1970) noted that the magnetic field of β CrB cannot be represented as a simple dipole and contains a geometry where one pole is stronger than the other. Stift (1975) explained that the shape of the longitudinal magnetic field (B_l) is not consistent with axisymmetric morphology,

★ E-mail: john.seach@usq.edu.au

and this was interpreted by Oetken (1977) as corresponding to a superposition of a dipole and a quadrupole magnetic field with their axes perpendicular to the rotation axis.

The lack of magnetic field symmetry around the rotation axis for β CrB is further discussed by Mathys (1993), and Mathys & Hubrig (1997) indicated that magnetic field is unusual and appears quite complex. A study of magnetic curves by Bagnulo et al. (2000) indicated that the magnetic topology of β CrB is characterized by a multipole expansion of a dipole and an arbitrarily oriented quadrupole. We include β CrB in this paper since it is one of the coolest magnetic Ap stars that is located close to the transition between fossil and dynamo magnetic fields. It provides a contrast with σ Boo that possibly is located on the cool side of the magnetic transition.

σ Boo was identified in our magnetic snapshot survey of F-type stars (Paper 1) as the hottest star in our sample having a possible dynamo magnetic field. Dynamo magnetic fields have been mapped on the surface of several late F-stars; see e.g. HR 1817, F7/8 (Marsden et al. 2006; Järvinen et al. 2015), τ Boo, F7V (Donati et al. 2008; Fares et al. 2009; Jeffers et al. 2018), HD 75332, F7V (Brown et al. 2021), HD 179949, F8V (Fares et al. 2012), θ Dra, F8IV, and β Vir, F9V (Paper 2). Mapping the surface magnetic field of σ Boo (F3V) is important for an understanding of magnetism in early F-stars close to the hot limit of dynamo magnetic fields and helps constrain dynamo models that provide insights into magnetism in stars with shallow outer convection zones.

2 OBSERVATIONS

2.1 Target selection

β CrB (HIP 75695) is a chemically peculiar (Adelman 1973), spectroscopic binary with component V magnitudes of 3.68 and 5.20 separated by 0.30 arcsec (Mason et al. 2001). The primary component has $T_{\rm eff} = 7980 \pm 180$ K, and the secondary component has $T_{\rm eff} = 6750 \pm 230$ K (Bruntt et al. 2010). The star was included in our earlier paper (Paper 1) and identified as a good target for magnetic mapping due to the availability of polarized spectra over multiple epochs.

σ Boo (HIP 71284), $T_{\rm eff} = 6720 \pm 144$ K (Gaia collaboration 2018), is a 1.6 ± 0.3 Gyr old (Casagrande et al. 2011) triple star system with component V magnitudes 4.50, 10.66, and 12.08, respectively (Mason et al. 2001). σ Boo is classified as a standard F2V star in the MK classification system (Johnson & Morgan 1953), while Samus et al. (2017) classify it as F3V. The star was detected as magnetic in our earlier magnetic snapshot survey (Paper 1). There has been increasing interest in σ Boo as a host F-type star used in exoplanet weather modelling (Segura et al. 2003; Godolt et al. 2019; Rushby, Shields & Joshi 2019; Schwieterman et al. 2019; Palubski, Shields & Deitrick 2020; Kaltenegger & Lin 2021).

2.2 Observations

Polarized spectra of β CrB were obtained from the PolarBase data base (Petit et al. 2014), which is a publicly available data base containing stellar data collected with the ESPaDOnS (Donati et al. 2006a) and NARVAL (Aurière 2003) high-resolution ($R = 65\,000$) spectropolarimeters. The β CrB data consist of 143 spectra from 2015 April 13 to 2018 July 28 (Table 1) obtained with the NARVAL spectropolarimeter at the Telescope Bernard Lyot (TBL) at the Observatoire du Pic du Midi, France. Observations of β CrB in 2015–2017 were obtained using both circularly polarized (Stokes V) and linear (Stokes UQ) polarized spectra, while observations in 2018 were only obtained in circular polarization. In this paper, we present magnetic maps using circular polarization only, whereas the linear polarization observations are left for future work.

We obtained polarized spectra for σ Boo using the ESPaDOnS spectropolarimeter at the Canada–France–Hawaii Telescope (CFHT) observing in Stokes V. The observations consist of 105 polarized spectra over 11 nights from 2021 May 18 to 28, corresponding to an estimated 1.2 rotational cycles (Tables 2 and A1).

3 MAGNETIC FIELD MEASUREMENTS

3.1 Magnetic Zeeman signatures

The line addition technique of least squares deconvolution (LSD; Donati et al. 1997, 2006b) is used to enhance the Stokes V signal, by combining thousands of individual lines into a single line with mean parameters. LSD profiles are created using line masks from VALD3 (Ryabchikova et al. 2015) where the masks contain the wavelength, depths, and effective Landé factors to be used for the LSD code. We normalized the LSD profiles with the values taken from the means of a typical line mask (Folsom et al. 2016). The number of lines used in LSD analysis varies from 17488 to 17652 for β CrB (Table 1) and 17646 to 17654 for σ Boo (Tables 2 and A1). For σ Boo, we added the nightly LSD profiles into a single mean profile that further enhances the SNR and enables a magnetic detection from an otherwise weak magnetic field. The time between the first and last exposure used in each mean LSD profile is less than 2 h which is less than 1 per cent of the estimated rotation period. This was short enough time-span to avoid smearing of the profiles.

We use the statistical criteria of FAP to determine whether the Stokes V profile has a magnetic signal, or whether the Null profile has a spurious signal (Donati, Semel & Rees 1992; Donati et al. 1997). The probability function of Abramowitz & Stegun (1964) is combined with Chi-square (χ^2) statistics inside and outside the spectral lines to give the probability of the Stokes V data differing from a zero magnetic field. The FAP is calculated to determine for the presence of a magnetic field and is defined as being definite if the FAP is smaller than 10^{-5}, marginal if FAP between 10^{-3} and 10^{-5}, and not detected if FAP is greater than 10^{-3}. The FAP is used to check for the presence of a magnetic field in addition to a measurement of the longitudinal magnetic field which is discussed in Section 3.2.

In Fig. 1, we compare two LSD profiles for β CrB at similar phases obtained in different years. The figure displays an LSD profile from 2015 April 23 at rotational phase 0.546, and a profile from 2017 March 8 at rotational phase 0.542. Zeeman signatures are visible in the Stokes V profiles which align with the Stokes I profile. The null spectrum does not show a magnetic signature and acts as a check to ensure that spurious signals have not contaminated the spectrum. The plots show almost identical Stokes V profiles that indicates a stable magnetic field over the 2 yr of observations. The longitudinal magnetic field strength (see Section 3.2) for the 2015 April profile 24 is -501.9 ± 6.2 G, while the value for 2017 March 8 is -496.7 ± 4.7 G. Magnetic signatures are visible in all 143 LSD profiles for β CrB and the FAP indicates a magnetic detection in all profiles.

In Fig. 2, we display an example of the mean Stokes V LSD profile for σ Boo on 2021 May 18. Due to the weak magnetic field, a Zeeman signature is not visible in individual LSD profiles, but is visible in the mean nightly profile due to the enhanced SNR. The FAP indicates a definite magnetic a magnetic detection in one of the mean LSD

Table 1. Journal of observations for β CrB in 2015–2018. Zero rotation cycle is set to our first observation on 2015 April 13. The table displays the date and time of the observation, zero rotation cycle with respect to the first observation on 2015 April 13, Stokes *I* profile, radial velocity (RV), longitudinal magnetic field (B_l), null value (N_l), and the number of lines used in LSD.

Date (UT)	Time (UT)	Mid-HJD 2457000+	Rot. cycle	SNR Stokes *I*	RV (km s^{-1})	B_l (G)	N_l (G)	LSD lines used
2015								
April 13	23:26:15	126.47656	0.000	264	−18.45	608.9 ± 5.9	− 1.6 ± 1.9	17 614
April 14	21:58:41	127.41575	0.051	294	−18.39	684.5 ± 7.6	5.4 ± 5.4	17 610
April 21	02:18:00	133.59583	0.385	280	−18.36	− 99.8 ± 4.4	1.4 ± 2.0	17 619
April 24	01:43:00	136.57153	0.546	270	−18.44	− 501.9 ± 6.2	− 1.3 ± 2.0	17 616
April 30	01:12:28	142.55032	0.870	267	−18.42	242.2 ± 4.8	0.2 ± 1.8	17 613
May 12	00:05:35	154.50388	1.516	277	−18.38	− 476.7 ± 6.3	5.0 ± 2.9	17 615
May 13	00:14:40	155.51019	1.571	271	−18.31	− 518.5 ± 6.5	− 4.0 ± 2.6	17 616
May 16	23:52:13	159.49459	1.786	279	−18.36	− 65.9 ± 5.0	− 0.4 ± 2.1	17 620
May 18	02:47:31	160.61633	1.847	285	−18.36	160.5 ± 5.0	1.9 ± 2.6	17 621
May 26	21:49:46	169.40956	2.322	272	−18.11	127.1 ± 4.1	− 1.4 ± 1.9	17 621
May 27	21:36:39	170.40045	2.376	277	−18.17	− 79.0 ± 4.4	0.2 ± 2.1	17 621
May 28	20:29:47	171.35402	2.428	278	−18.21	− 267.4 ± 5.0	1.2 ± 2.2	17 617
May 31	02:37:08	173.60912	2.550	269	−18.24	− 513.3 ± 6.2	− 1.9 ± 2.0	17 615
2016								
August 6	20:15:33	607.34413	26.011	293	−17.38	620.1 ± 5.4	0.6 ± 1.6	17 616
August 7	20:19:40	608.34699	26.066	293	−17.31	685.2 ± 5.6	2.0 ± 1.5	17 617
August 8	20:10:53	609.34089	26.119	291	−17.28	676.5 ± 5.5	1.3 ± 1.6	17 617
August 10	20:10:22	611.34053	26.228	299	−17.27	419.5 ± 4.7	− 1.9 ± 1.9	17 617
August 11	20:04:07	612.33619	26.281	295	−17.26	224.4 ± 4.2	0.7 ± 1.9	17 616
August 12	20:10:37	613.34071	26.336	300	−17.29	14.2 ± 4.4	− 1.0 ± 2.6	17 616
August 18	19:53:21	619.32872	26.660	292	−17.42	− 427.6 ± 6.0	− 2.3 ± 2.8	17 618
August 21	19:55:18	622.33007	26.822	290	−17.40	57.3 ± 4.4	0.2 ± 2.0	17 616
August 22	21:17:33	623.38719	26.879	292	−17.39	265.4 ± 4.9	− 1.5 ± 2.8	17 615
August 23	21:15:09	624.37858	26.933	290	−17.37	440.0 ± 5.0	2.3 ± 2.2	17 615
August 24	21:11:05	625.38270	26.987	292	−17.35	578.1 ± 5.4	0.1 ± 2.0	17 617
2017								
March 2	01:58:41	814.58242	37.221	300	−17.22	440.7 ± 7.5	− 0.4 ± 6.4	17 619
March 8	00:06:05	820.50422	37.542	288	−17.35	− 496.7 ± 4.7	− 2.3 ± 4.8	17 621
March 15	02:01:08	827.58412	37.925	291	−17.33	441.4 ± 4.7	− 1.8 ± 0.8	17 620
March 16	00:15:13	828.51057	37.975	297	−17.32	589.7 ± 5.4	− 0.5 ± 0.5	17 620
March 17	04:26:03	829.68476	38.038	297	−17.29	697.3 ± 5.5	− 0.1 ± 0.5	17 620
March 18	05:17:31	830.72050	38.094	303	−17.29	728.5 ± 5.8	− 0.2 ± 0.5	17 621
March 19	04:03:40	831.66921	38.146	295	−17.18	658.5 ± 5.5	1.0 ± 0.5	17 622
March 20	04:10:28	832.67394	38.200	296	−17.17	525.0 ± 4.9	0.1 ± 0.6	17 620
March 29	02:03:06	841.58549	38.682	286	−17.39	− 375.1 ± 5.4	0.6 ± 1.9	17 619
March 29	02:43:57	841.61385	38.684	290	−17.38	− 385.3 ± 5.2	0.2 ± 0.5	17 618
March 30	01:28:42	842.56160	38.735	292	−17.39	− 240.0 ± 5.3	− 4.4 ± 2.8	17 617
March 30	02:16:17	842.59464	38.737	296	−17.40	− 235.6 ± 4.7	0.2 ± 0.8	17 617
April 3	01:21:32	846.55662	38.951	316	−17.36	513.5 ± 4.7	0.1 ± 0.8	17 620
April 4	01:00:20	847.54190	39.004	297	−17.34	7.2 ± 0.1	0.0 ± 0.0	17 620
April 4	01:10:46	847.54914	39.005	292	−17.35	646.7 ± 5.3	− 0.5 ± 0.4	17 620
April 7	00:55:54	850.53882	39.166	300	−17.21	616.4 ± 5.3	0.3 ± 0.6	17 622
April 8	00:40:43	851.52828	39.220	297	−17.20	460.4 ± 4.6	0.4 ± 0.6	17 622
April 9	02:15:17	852.59395	39.278	336	−17.21	227.9 ± 4.4	4.5 ± 2.6	17 620
April 9	02:25:07	852.60078	39.278	325	−17.21	248.0 ± 3.8	0.0 ± 0.6	17 621
April 11	03:24:33	854.64205	39.388	301	−17.29	− 144.0 ± 4.4	0.6 ± 0.7	17 623
April 12	02:29:46	855.60400	39.440	298	−17.31	− 376.7 ± 4.9	0.2 ± 0.5	17 620
April 13	03:00:24	856.62528	39.496	298	−17.32	− 497.8 ± 5.6	0.3 ± 0.5	17 623
April 16	03:27:12	859.64389	39.659	290	−17.43	− 439.7 ± 5.5	− 0.3 ± 0.5	17 623
April 17	03:47:30	860.65799	39.714	291	−17.37	− 308.7 ± 4.9	− 1.1 ± 0.5	17 620
April 18	01:18:22	861.55442	39.762	293	−17.37	− 153.0 ± 4.4	− 1.1 ± 0.5	17 620
April 20	02:31:18	863.60507	39.873	297	−17.44	256.6 ± 4.2	0.7 ± 0.9	17 620
April 21	01:54:56	864.57981	39.926	296	−17.37	451.7 ± 4.6	− 0.6 ± 0.5	17 621
April 23	02:21:19	866.59814	40.035	294	−17.31	694.7 ± 5.6	− 0.3 ± 0.5	17 618
April 24	01:48:26	867.57530	40.088	297	−17.26	726.7 ± 5.6	− 0.1 ± 0.4	17 615
2018								
April 14	00:00:38	222.50044	59.287	297	−17.47	4.3 ± 4.5	− 3.2 ± 3.0	17 623
April 18	03:36:14	226.65016	59.511	285	−17.54	− 442.7 ± 6.5	4.7 ± 4.4	17 623
April 19	03:46:04	227.65699	59.566	278	−17.54	− 471.5 ± 6.4	2.7 ± 3.7	17 621
April 24	01:24:37	232.55876	59.831	289	−17.53	61.4 ± 4.7	2.9 ± 3.3	17 617

Table 1 – *continued*

Date (UT)	Time (UT)	Mid-HJD 2457000+	Rot. cycle	SNR Stokes *I*	RV (km s^{-1})	B_l (G)	N_l (G)	LSD lines used
April 24	23:55:42	233.49701	59.882	292	−17.53	203.4 ± 4.7	−4.8 ± 3.6	17 618
May 6	00:27:09	244.51885	60.478	295	−17.52	−423.7 ± 5.7	11.2 ± 2.7	17 618
May 11	00:29:12	249.52028	60.748	298	−17.57	−198.5 ± 5.7	−6.7 ± 2.5	17 623
May 17	01:12:33	255.55038	61.075	289	−17.42	703.3 ± 6.2	0.5 ± 2.4	17 627
June 14	23:45:34	284.48998	62.640	276	−17.59	−462.4 ± 5.9	−1.6 ± 1.9	17 631
June 16	23:13:21	286.46760	62.747	289	−17.65	221.7 ± 5.0	1.2 ± 2.1	17 629
June 17	23:34:11	287.48207	62.802	286	−17.65	−32.8 ± 4.5	1.2 ± 2.1	17 629
June 18	22:55:32	288.45523	62.855	278	−17.64	246.5 ± 6.1	−2.3 ± 4.5	17 629
June 19	21:26:50	289.39363	62.905	288	−17.62	343.9 ± 4.8	−3.8 ± 2.4	17 629
June 24	23:17:23	294.47041	63.180	296	−17.49	564.5 ± 5.6	0.9 ± 2.7	17 650
June 25	22:35:44	295.44148	63.232	279	−17.49	413.7 ± 5.4	−3.5 ± 3.4	17 652
June 30	22:24:02	300.43336	63.502	226	−17.64	−236.0 ± 70.0	−80.3 ± 30.6	17 488
July 9	22:42:15	309.44601	63.990	273	−17.52	571.9 ± 5.5	0.9 ± 1.8	17 637
July 22	23:17:37	322.47057	64.694	271	−17.63	−336.8 ± 6.0	2.5 ± 2.4	17 642
July 23	20:58:50	323.37419	64.743	277	−17.62	−182.9 ± 5.9	−3.9 ± 3.3	17 641
July 26	21:14:16	326.38491	64.906	277	−17.59	420.6 ± 5.5	−3.6 ± 2.8	17 642
July 28	21:03:31	328.37744	65.014	273	−17.55	670.0 ± 6.3	8.8 ± 2.4	17 642

Table 2. Journal of observations for σ Boo in 2021. The table displays the date of the observation, number of LSD profiles combined in the mean profile, zero rotation cycle with respect to the first observation on 2021 May 18, Stokes *I* profile mean SNR, RV, longitudinal magnetic field (B_l), null value (N_l), and magnetic detection flag for the presence of a magnetic field in the mean LSD profiles, where D is a definite detection, M is marginal, and N is no detection calculated using the false alarm probability (FAP). HJD are the mean values of the nightly observations. Rotation cycle is displayed as the mean time of observation for each night. A journal of the individual observations is shown in the appendix.

Date (UT)	Mid-HJD 2459000+	No. LSD profiles	Rot. cycle	SNR Stokes *I*	RV (km s^{-1})	B_l (G)	N_l (G)	Det. N, M, D
May 18	352.82771	12	0.000	2468	0.29 ± 0.01	−1.0 ± 0.2	−0.1 ± 0.2	M
May 19	353.80843	12	0.117	2515	0.34 ± 0.01	−0.7 ± 0.1	0.1 ± 0.2	M
May 20	354.82750	12	0.238	2528	0.34 ± 0.01	−0.7 ± 0.2	−0.4 ± 0.2	D
May 21	355.77625	12	0.351	2171	0.32 ± 0.01	−1.4 ± 0.6	−1.0 ± 0.6	M
May 22	356.74181	3	0.466	1048	0.37 ± 0.01	−2.5 ± 1.0	−0.6 ± 1.2	N
May 24a	358.81633	6	0.713	1609	0.35 ± 0.01	−1.1 ± 0.3	0.0 ± 0.3	N
May 24b	358.94385	6	0.728	1640	0.35 ± 0.01	−1.1 ± 0.4	0.1 ± 0.4	N
May 25	359.81721	6	0.832	1607	0.35 ± 0.01	−0.6 ± 0.2	−0.4 ± 0.3	N
May 26	360.92690	12	0.964	2353	0.30 ± 0.01	−0.4 ± 0.2	0.1 ± 0.2	M
May 27	361.77358	12	1.065	2425	0.36 ± 0.01	−0.3 ± 0.1	−0.2 ± 0.1	N
May 28	362.77587	12	1.184	2369	0.32 ± 0.01	−0.7 ± 0.2	−0.4 ± 0.2	M

profiles, marginal detection in five profiles, and no detection in five profiles (Table 2).

3.2 Longitudinal magnetic field

We determine the longitudinal magnetic field (B_l) according to Donati et al. (1997),

$$B_l = -2.14 \times 10^{11} \frac{\int v V(v) \mathrm{d}v}{\lambda g c \int [I_c - I(v)] \mathrm{d}v}, \quad (1)$$

where B_l is the longitudinal magnetic field in gauss, λ is the mean wavelength of all lines used to calculate the LSD profile in nm, g is the mean value of the Landé factors of all lines used to construct the LSD profile, c is the speed of light (in the same units as v), and I_c is the continuum level of the intensity profile. B_l is defined as the line-of-sight component of the field, which is averaged over the visible stellar disc (Babcock 1947; Schwarzschild 1950), and according to Mathys (1989) and Donati et al. (1997) is measured from the first-order moment of the Stokes *V* LSD profile. As a first-order approximation B_l is considered to be proportional to the shift in wavelength between left and right circularly polarized lines (Mathys 1995).

Stars with a fossil magnetic field are expected to be stable over long periods of time and show smooth sinusoidal rotational modulation of B_l that changes polarity over the rotation cycle as the positive and negative magnetic poles become visible. In contrast, dynamo magnetic fields are complex and dynamic and are not expected to show rotational modulation of B_l synchronized with the rotational cycle over longer periods of time due to evolution of the magnetic field.

We apply a generalized Lomb–Scargle periodogram (GLS; Zechmeister & Kürster 2009) to search for a period in the time-series of B_l measurements. We also calculate the FAP (Baluev 2008), which quantifies the probability of the maximum peak being produced by a signal without a periodic component (VanderPlas 2018). A plot of power versus frequency in Fig. 3 shows a peak with an FAP $> 10^{-9}$ corresponding to an excellent fit of the sine curve to the data. This peak with maximum power corresponds to sine curve with a period of 18.4748 d, which is consistent with the equatorial rotation period of 18.5 d found by Preston (1967a), 18.497 d (Steinitz 1967),

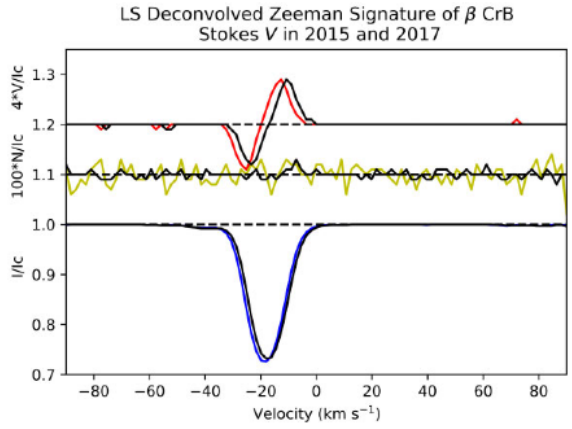

Figure 1. Comparison of two LSD profiles for β CrB at similar phases in different years. The LSD profile from 2015 April 24 at rotational phase 0.546 is displayed with the upper red line showing the Stokes V profile (y-axis expanded 4× and shifted up by 0.2 to allow better visibility). The middle green-yellow line shows the null profile (expanded 100× and shifted up by 0.1). The lower blue line shows the Stokes I profile. The profile from 8 March 2017 at rotational phase 0.542 is overplotted in black. The two plots show almost identical Stokes V profiles and a stable magnetic field over the 2 yr of observations, showing the well-known observation that β CrB contains a fossil magnetic field. The zero rotation phase for both figures is aligned to our first observation of β CrB on 2015 April 13.

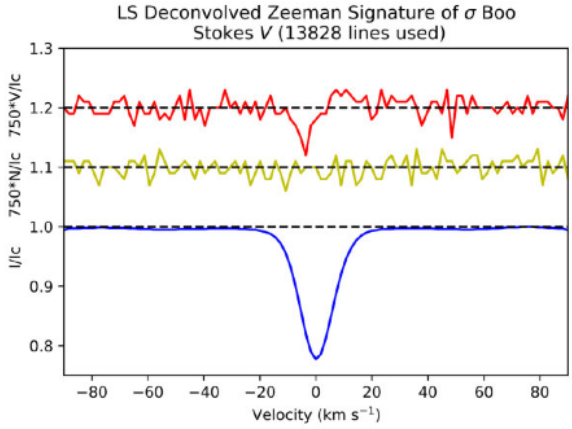

Figure 2. Mean LSD profile for σ Boo on 2021 May 18. The upper line (red) shows the Stokes V profile (y-axis expanded by 750 times and shifted up by 0.2 to allow better visibility). The middle line (green-yellow) shows the null profile (expanded by 750 times and shifted up by 0.1), which is used as a check for any spurious signals contaminating the spectra. The lower line (blue) shows the Stokes I profile.

18.4868 d (Kurtz 1989; Leroy 1995), and 18.4866 d (Bagnulo et al. 2000). We compute the window function (VanderPlas 2018) that is a check for the presence of periods caused by observational biases in the data. The window function is determined by applying a Lomb–Scargle periodogram to the data with the B_l measurements set to 1. The window function is shown in Fig. 3 and indicates there are no patterns in the timing of observations.

We determine 143 B_l values for β CrB over a 4-yr period between 2015 and 2018 (Table 1). A plot of the rotational modulation of B_l (Fig. 4) shows a sinusoidal curve that results from both positive and negative magnetic poles being visible over the rotation cycle. B_l spans a range of values from $+751.6 \pm 5.8$ G at phase 0.08 to -528.8 ± 6.8 G at phase 0.57 that is consistent with the range found by previous studies (Wade et al. 2000; Leone & Catanzaro 2001). Fig. 4 shows the rotational modulation B_l for each epoch which remains stable over the 4 yr of observations that is consistent with the behaviour of a fossil field.

We apply a GLS periodogram to the B_l measurements of σ Boo from 2021 May 18 to 28 (Tables 2 and A1), and find a sine period of 7.7 ± 1.0 d with an FAP of approximately 0.1 (Fig. 5). The window function is shown in Fig. 5, and indicates there are no patterns in the timing of observations. A plot of the rotational modulation of 11 mean nightly values of B_l for σ Boo is shown in Fig. 6, where we overlay a sinusoidal curve with a period that corresponds to an estimated stellar rotation period of 8.4 ± 0.2 d determined from ZDI χ^2 minimization (Table 4). The plot of B_l versus rotation phase shows a possible rotational modulation of the magnetic field; however, the large error bars make the determination uncertain.

4 MAGNETIC FIELD MODELLING

4.1 Longitudinal field modelling

The oblique rotator model (Babcock 1949; Stibbs 1950; Deutsch 1958, 1970; Pyper 1969; Falk & Wehlau 1974) is a useful first step in modelling the longitudinal magnetic field of a hot star where the field is considered to be a simple dipole inclined to the rotation axis. We derive the geometry and strength of the dipole fossil field of β CrB using parameters: inclination of the rotational axis with respect to the observer (i), obliquity of the dipole axis with respect to the rotational axis (β) counted from the positive rotational pole towards the positive magnetic pole, and the polar strength of the surface magnetic field (B_d) calculated at the positive magnetic pole. Following the oblique rotator model of Preston (1967b):

$$\beta = arctan\left[\left(\frac{1-r}{1+r}\right) - \cot i\right], \tag{2}$$

where

$$r = \frac{B_l(min)}{B_l(max)} = \frac{\cos\beta\cos i - \sin\beta\sin i}{\cos\beta\cos i + \sin\beta\sin i}. \tag{3}$$

We calculate the polar field strength (B_d) of following the relation given by Blazère et al. (2020),

$$B_d = B_{max}\left(\frac{15+u}{20(3-u)}(\cos\beta\cos i + \sin\beta\sin i)\right)^{-1} \tag{4}$$

where we use the limb-darkening coefficient $u = 0.57$ from Gray (2005), B_l max $= +751.6 \pm 5.8$ G and B_l min $= -528.8 \pm 6.8$ G calculated from fitting a sinusoidal curve to the data in Fig. 3. The value for $r = 0.70 \pm 0.006$ is calculated using equation (3). The value for $i = 39 \pm 4$ deg is calculated from the mean epoch values determined from ZDI χ^2 minimization, and $\beta = 26 \pm 4$ deg from the mean epoch values calculated using equation (2). We calculate the polar field strength (B_d) of β CrB $= 2423 \pm 51$ G. The values are presented in Table 3.

Schwarzschild (1950) showed the maximum value for a longitudinal magnetic field (B_l) is 30 per cent of the dipolar field. Our B_l max value of $+751.6 \pm 5.8$ G is 31.0 per cent of our calculated B_d of 2423 ± 51 G, which is consistent with Schwarzschild's prediction.

Landstreet & Mathys (2000) and Bagnulo et al. (2002) suggest the dipolar field obliquity (β) is correlated with stellar rotational period, where low-β geometries are more common in slow rotators. Landstreet & Mathys (2000) indicate that stars with rotation periods of about one month have their magnetic and rotation axes aligned within about 20 deg of each other, while faster rotating stars have

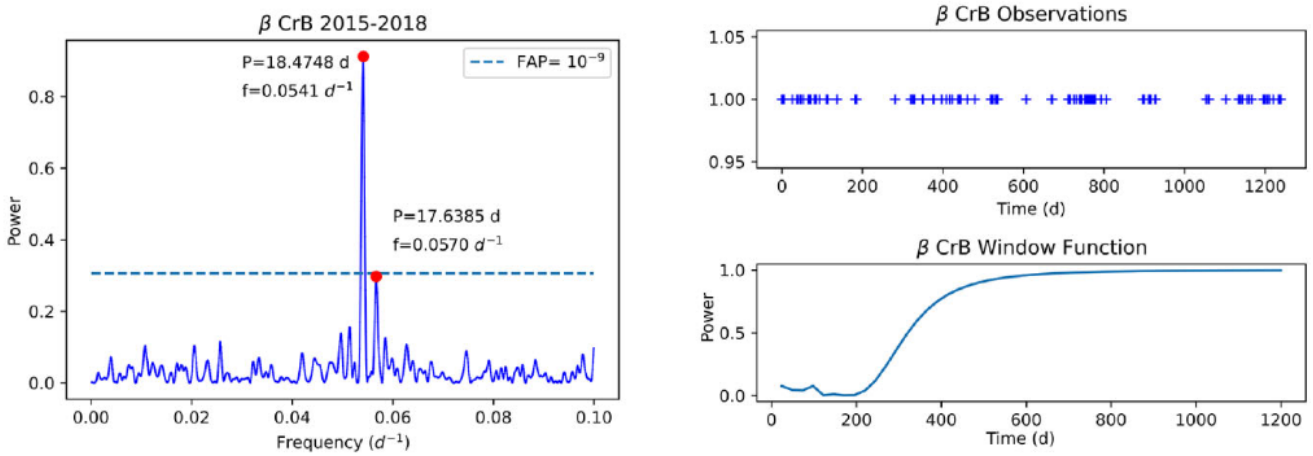

Figure 3. Figure at left: GLS periodogram a time-series of B_l measurements for β CrB spanning 1240 d from 2015 March 7 to 2018 July 28 (Table 1). The figure shows the power versus frequency and FAP, with the highest peaks marked with a red circle, and text describing the associated period and frequency. The FAP quantifies the probability of the maximum peak being produced by a signal without a periodic component. The blue dashed line is FAP 10^{-9} level, which indicates an excellent detection for the period determination. The best sine period determined from the GLS periodogram is 18.4748 ± 0.005 d. The figure at top right shows the time spacing of the observations. Figure at bottom right shows the window function.

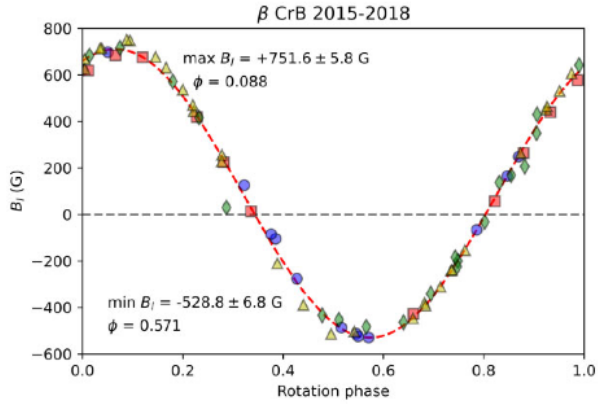

Figure 4. The figure shows the rotational modulation of B_l for β CrB from 73 observations corresponding to magnetic maps from 2015 to 2018. The data from 2015 are shown as blue circle, 2016 red square, 2017 yellow triangle, and 2018 green diamond. The dashed red curve indicates a fitted sine curve to the data with a period period of 18.4868 d that corresponds to the rotation period used in ZDI analysis. The rotation phase ϕ corresponds to the measured maximum and minimum B_l. The figure shows the magnetic field is stable over the 4 yr observation period. The zero day is the first date of B_l measurement on 2018 January 23.

larger values of β. Since β CrB is a slow rotator with a period of 18.5 d (Section 3.2), we may expect that β will be larger 20 deg. We determine β values of 29 ± 3 deg, using equation (2) and 26 ± 4 deg from ZDI χ^2 minimization Section 4.2, which is consistent with the trend from Landstreet & Mathys (2000).

4.2 Zeeman Doppler imaging

The surface magnetic fields of β CrB and σ Boo are reconstructed using the inversion technique of ZDI (Semel 1989; Donati & Brown 1997), using a spherical harmonics expansion of the surface magnetic field (Donati et al. 2006b). Recovery of reliable maps depends on modelling Stokes *I* and *V* profiles and using a model local line profile. ZDI involves an iterative procedure that begins with a zero magnetic field, and parameters are adjusted to optimize the fit (parametrized by reduced χ^2) of the model compared to observations. The local line profile is an approximation to the actual line profile (Piskunov & Rice 1993) and is the function used to calculate the line at one point on the surface of the star. We modelled the local line profile using a Voigt profile (Table 4).

We assume the model star is spherical and divided into approximately equal area surface elements with coordinates of colatitude and longitude. Colatitude increases with distance from the north pole, and longitude increases in the direction of rotation, with the coordinate system aligned with the stellar rotation axis. We use a stellar surface divided into a 4584 point grid, with 120 spatially resolved elements around the equator, and 60 in colatitude similar to Folsom et al. (2018). The minimum χ^2 used in the ZDI code is determined by running the code with increasing values and finding the χ^2 value where there is no increase in magnetic energy as used in Paper 2. Using this method, we adopt a χ^2 of 4.0 for β CrB and 0.95 for σ Boo.

For β CrB, the local line width used are Gaussian width 2.41 km s^{-1}, Lorentzian width 0.89 km s^{-1}, and limb darkening coefficient 0.57. The wavelength 512.6 nm and effective Landé factor 1.195 used for computing Stokes *V* are the normalizing values for the LSD profile. For σ Boo, the local line width used are Gaussian width 2.41 km s^{-1}, Lorentzian width 0.89 km s^{-1}, and limb darkening coefficient 0.70. The wavelength 512.6 nm and effective Landé factor 1.195 used for computing Stokes *V* are the normalizing values for the LSD profile. The profiles for both stars are convolved with a Gaussian instrumental profile of $R = 65\,000$.

4.2.1 *Modelling the LSD stokes profiles*

The Stokes *V* maximum entropy fit for β CrB is shown in Fig. 7. The plot shows a good fit between the observed and modelled profiles that adds weight to the reliability of our magnetic map reconstruction. The Stokes *V* LSD profile for σ Boo (Fig. 2) is produced by co-adding the nightly LSD profiles, which further increases the SNR of the weak magnetic field. The Stokes *V* maximum entropy fit for σ Boo is shown in Fig. 8. The plot shows a moderate fit between the observed and modelled profiles.

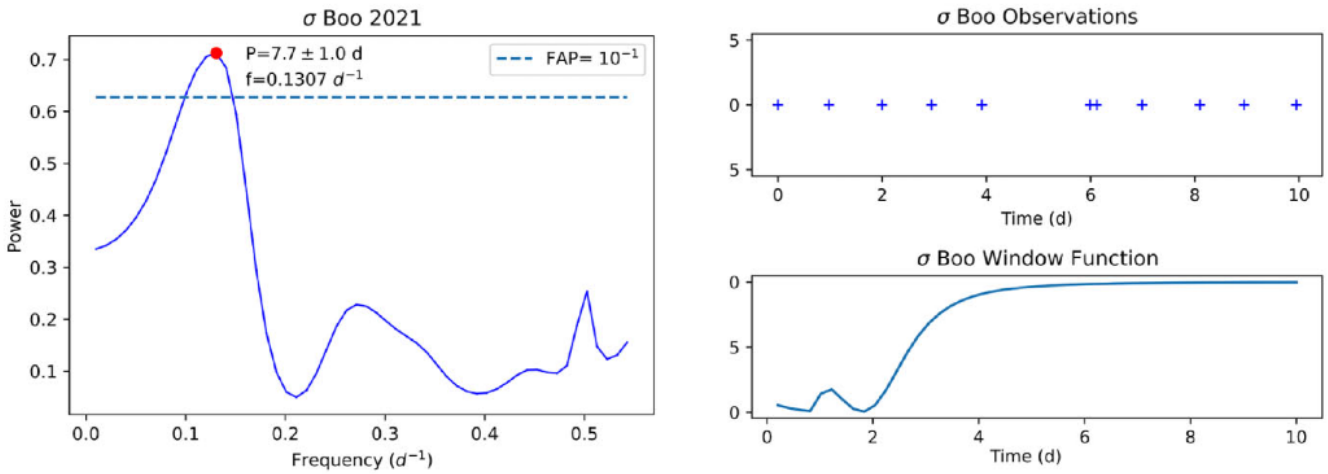

Figure 5. Figure at left: GLS periodogram a time-series of B_l measurements for σ Boo spanning 11 d from 2021 May 18 to 28 (Table 2). The figure shows the power versus frequency and FAP, with the highest peak marked with a red circle, and text describing the associated period and frequency. The blue dashed line is FAP 10^{-1} level. The best sine period determined from the GLS periodogram is 7.7 ± 1.0 d. The figure at top right shows the time spacing of the observations. Figure at bottom right shows the window function.

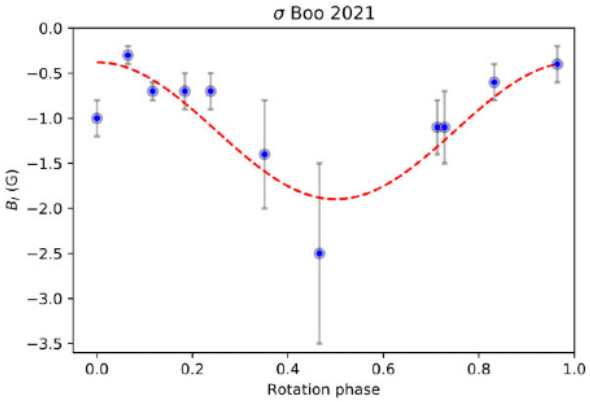

Figure 6. Figure shows the rotational modulation of B_l for σ Boo from 11 observations in 2021 May from the mean LSD profiles from each night. The red dashed line indicates a fitted sine curve to the data with a period of 8.4 d corresponding to an estimated stellar rotation period determined from ZDI.

4.2.2 β CrB magnetic maps

The large-scale magnetic field topology for β CrB at six epochs are shown in Fig. 9. The stellar parameters used to reconstruct the map are determined using a method of χ^2 minimization (Petit, Donati & Collier Cameron 2002) whereby we iteratively change individual parameters and re-run ZDI analysis, to find the parameter with the minimum χ^2 when we fit a Gaussian curve to the χ^2 values. The formal uncertainties in parameter estimation are determined by finding the 1σ uncertainty around Gaussian fit to the χ^2 minimization. The parameters determined by ZDI analysis of each magnetic map are shown in Table 4.

We adopt the same stellar parameters for all β CrB maps displayed in Table 4 that are mean $v \sin i = 9.4$ km s^{-1}, mean inclination = 39 deg, and differential rotation $d\Omega = 0.0$ rad d^{-1}. The mean and 1σ errors are derived from the mean values averaged over the six maps. For P_{rot}, we use the value of 18.4868 d from Kurtz (1989) since this value is within the uncertainty of our ZDI determination of 18.59 ± 0.07 d. The spherical harmonic expansion is limited to $\ell_{max} = 20$ since no further detail is obtained with higher degrees. The rotation phase of all maps is aligned to a common zero date, with the first observation date set to MJD = 2457126.47656 (2015 April 13). The data sets comprise between 8 and 15 LSD profiles (Table 3).

The large-scale magnetic features are similar on all maps and indicate that the field is stable over the 39 month observation period. This is consistent with the fossil field nature of β CrB where the field remains frozen into the stellar atmosphere and is expected to remain unchanged over a long period of time. The radial magnetic field shows a large area of negative polarity in the mid-northern latitudes between phases 0.2–0.6 and a region of positive magnetic field in the northern latitudes between phases 0.8–1.0. The azimuthal magnetic field shows a region of negative polarity that approximately matches the position of negative radial field between 0.2–0.6, and a small region of positive field with strengths of about 1000–2000 G at the north pole.

The complexity of the surface magnetic field for β CrB is quantified by calculating the fractional strength of the magnetic field components that are displayed in Table 5. The calculated percentages from the Stokes V maps are the average squared magnetic field $\langle B^2 \rangle$, which is proportional to the magnetic energy (Reiners 2012). The uncertainties are derived by varying the stellar parameters over the 1σ errors for each individual parameter, and taking the extreme values of the results as the variation. The dominant term in the spherical harmonics expansion is the dipole ($\ell = 1$), which ranges from 50^{+5}_{-0} to 61^{+0}_{-9} per cent over the six epochs from 2015 to 2018. The second largest spherical harmonics term is the quadrupole ($\ell = 2$) with 18^{+2}_{-1} to 21^{+0}_{-4} per cent of magnetic energy. The octupole ($\ell = 3$) contains between 5^{+1}_{-0} and 7^{+0}_{-2} per cent of magnetic energy. The higher multipoles ($\ell > 3$) contain a significant fraction of magnetic energy with 12^{+13}_{-0} to 27^{+0}_{-5} per cent of magnetic energy.

The maximum magnetic field strength of our magnetic map of β CrB, $B_{max} = 4106$ G for the 2017 April 7–24 map, which also has the highest $B_{mean} = 1192$ G. In contrast, the maximum B_l is only +728.5 G. This large difference between B_{max} and B_l values indicates a significant transverse magnetic field component may be present in β CrB, resulting in magnetic flux cancellation. This flux cancellation is consistent with a complex magnetic field structure on the surface of β CrB. The magnetic field configuration is predominately poloidal with values ranging from 73 to 90 per cent (Table 5). The uncertainties are derived by varying the stellar parameters over the 1σ errors for each individual parameter, and taking the extreme values of the results as

Table 3. Stellar parameters for β CrB between 2015 and 2018, and σ Boo in 2021 determined from our ZDI analysis. For β CrB, polar field strength (B_d) and obliquity angle (β) are calculated from a dipole model of the star ($\ell_{max} = 1$). β_{ORM} is calculated from the oblique rotator model using equation (2). β_{ZDI} is calculated using ZDI. B_d is calculated from equation (4) using β from equation (2) and inclination from ZDI χ^2 minimization. Maximum dipolar field strength from ZDI output. For σ Boo, the 11 mean LSD profiles constructed from 105 individual profiles.

Epoch (UT)	Obs. rot cycles	No. LSD profiles	Incl. (deg)	$v \sin i$ (km s^{-1})	Eq rot period (d)	Obliquity angle β_{ORM} (deg)	Obliquity angle β_{ZDI} (deg)	Polar field str. B_d (G)	Dipolar max (G)
β CrB									
13 Apr–30 May 2015	2.5	13	35 ± 2	9.2 ± 0.2	18.475 ± 0.102	32 ± 2	32	2364	1389^{+52}_{-30}
6–24 Aug 2016	1.0	11	35 ± 2	9.8 ± 0.2	18.450 ± 0.020	32 ± 2	22	2364	1469^{+0}_{-110}
2 Mar–4 Apr 2017	0.9	15	42 ± 2	9.1 ± 0.3	18.465 ± 0.020	26 ± 2	21	2481	1406^{+35}_{-47}
7–24 Apr 2017	0.9	14	35 ± 2	9.2 ± 0.2	18.410 ± 0.021	32 ± 2	25	2401	1533^{+0}_{-173}
14 Apr–16 May 2018	1.8	8	46 ± 2	9.6 ± 0.2	18.625 ± 0.022	23 ± 2	28	2489	1281^{+160}_{-0}
14 Jun–28 Jul 2018	2.4	13	39 ± 2	9.4 ± 0.2	18.525 ± 0.022	28 ± 2	25	2440	1339^{+102}_{-0}
Mean	–	–	39 ± 4	9.4 ± 0.2	18.592 ± 0.069	29 ± 3	26 ± 4	2423 ± 51	1403 ± 82
σ Boo									
18–28 May 2021	1.2	11	15 ± 3	3.8 ± 0.3	8.4 ± 0.2	–	20	–	0.8

Table 4. Parameters used to produce the maximum-entropy image reconstructions for β CrB and σ Boo. β CrB P_{rot} from Kurtz (1989).

Parameter	β CrB	σ Boo
ZDI parameters		
Inclination (deg)	39 ± 4	15 ± 3
$v \sin i$ (km s^{-1})	9.4 ± 0.2	3.8 ± 0.3
P_{rot} (this work) (d)	18.50 ± 0.07	8.4 ± 0.2
P_{rot} (literature) (d)	18.4868	–
dΩ (rad d^{-1})	0.0	0.0
χ^2	4.0	0.95
degree ℓ_{max}	20	8

the variation. The parameter ranges used for β CrB are: inclination $\pm$ 4 deg, $v \sin i \pm 0.2$ km s^{-1}, and $P_{rot} \pm 0.07$ d. The Stokes V LSD fits to the observations are shown in Fig. 7 that indicates an excellent match between the observed Zeeman signatures and modelled line profiles, which adds further evidence of the reliability of our reconstructed magnetic maps.

4.2.3 *σ Boo magnetic map*

The large-scale magnetic field topology for σ Boo in 2021 May is shown in Fig. 10. The stellar parameters used to reconstruct the maps are determined using a method of χ^2 minimization as described in Section 4.2.2 are $v \sin i = 3.8$ km s^{-1}, inclination = 15 deg, rotation period = 8.4 d, and dΩ = 0.0 rad d^{-1}. The spherical harmonic expansion is limited to $\ell_{max} = 8$ since no further details are observed in the maps with higher degrees. The large-scale magnetic field shows a simple topology, which may partly be due to a low $v \sin i$ of 3.8 ± 0.3 km s^{-1} where the resolution is affected by the number of resolution elements (Morin et al. 2010).

The radial field of σ Boo shows a large region of negative polarity in the Northern hemisphere, with a maximum strength of 1.5 G at rotation phase 0.2–0.4. The positive magnetic pole is not visible on the map since it is located near the south polar region in an area that is tilted away from the observer. The azimuthal magnetic field shows mostly weak positive polarity (<0.5 G) that covers most of the surface except of a weak negative patch in the Northern hemisphere between phases 0.5–0.8. The meridional magnetic field shows mostly weak negative polarity (>−0.5 G) that covers most of the surface except of a positive patch at the north pole, and a negative area of approximately −1.0 G in the Northern hemisphere between phases 0.7–1.0.

The simplicity of the surface magnetic field of σ Boo is further indicated by the fractional strength of the magnetic field components that are displayed in Table 5. The dominant term in the spherical harmonics expansion is the dipole ($\ell = 1$) which contains 84 ± 1 per cent of the magnetic energy. The second largest spherical harmonics term is the quadrupole ($\ell = 2$) with 14 ± 1 per cent of the magnetic energy. The octupole ($\ell = 3$) contains between 2^{+0}_{-0} per cent of magnetic energy, while the higher order multipoles ($\ell > 3$) contain 2^{+1}_{-2} per cent of magnetic energy. The uncertainties are derived by varying the stellar parameters over the 1σ errors for each individual parameter and taking the extreme values of the results as the variation. The parameter ranges used for σ Boo are: inclination $\pm$3 deg, $v \sin i \pm 0.3$ km s^{-1}, $P_{rot} \pm 0.2$ d.

The maximum magnetic field strength of our magnetic map of σ Boo, $|B_{max}|$ =1.5 G that is consistent with the expected weak magnetic fields for F-type stars (Marsden et al. 2014) and Paper 1. The magnetic field for σ Boo is mainly poloidal which is consistent with the finding of Petit et al. (2008) who found that stars with P_{rot} < 12 d are more likely to have increasing proportion of magnetic energy in the poloidal field. The simple magnetic topology of σ Boo is similar to the slow rotating ($v \sin i = 6.1$ km s^{-1}) F9V star β Vir (Paper 2) that also has a mainly poloidal field with a weak magnetic field (B_{max}=1.6 G).

4.3 Differential rotation

An understanding of differential rotation (dΩ) in hot stars, and the conditions of the atmosphere are incomplete; however, there is evidence from Kepler photometric data that rotational shear is present in about 60 per cent of A-type stars, compared to 75 per cent of F-stars, and 95 per cent of G-stars (Balona & Abedigamba 2016). We do not find evidence of dΩ in β CrB using the method of χ^2 minimization as described in Section 4.2.2. The lack of detected dΩ is consistent with the suggestion that hot stars with strong magnetic fields maintain uniform rotation along field lines (Mathis & Zahn 2005; Zahn 2010). The presence of dΩ in hot stars is also strongly

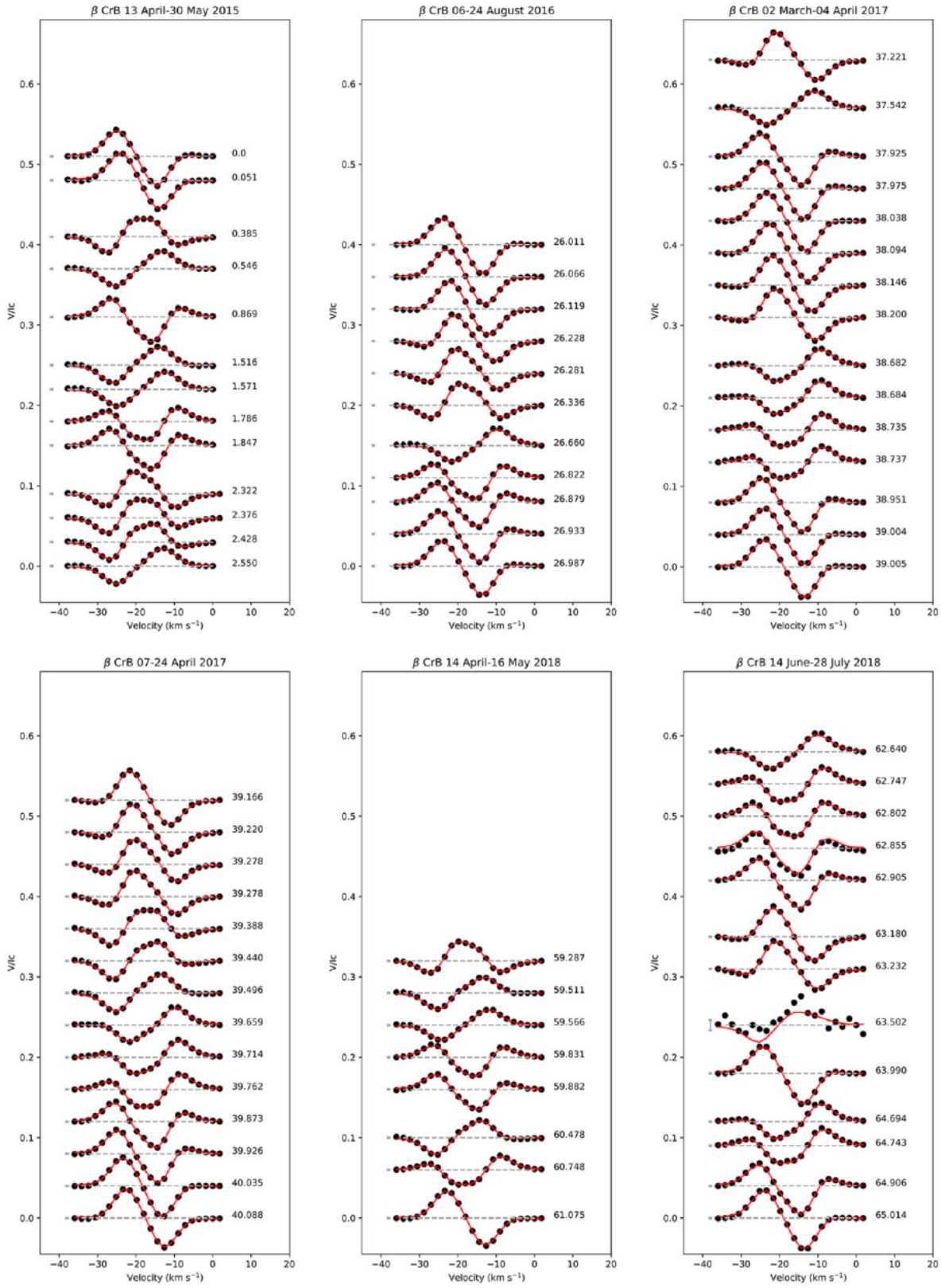

Figure 7. Stokes *V* fit for β CrB corresponding to 2015–2108 magnetic maps. The black lines represent the observed Zeeman signatures, while the red lines represent the modelled line profiles. The 1σ error bars are very small and are shown on the left. The line profiles are arranged vertically by rotation cycle and separated to allow better visibility. The rotation cycle is shown on the right of each profile.

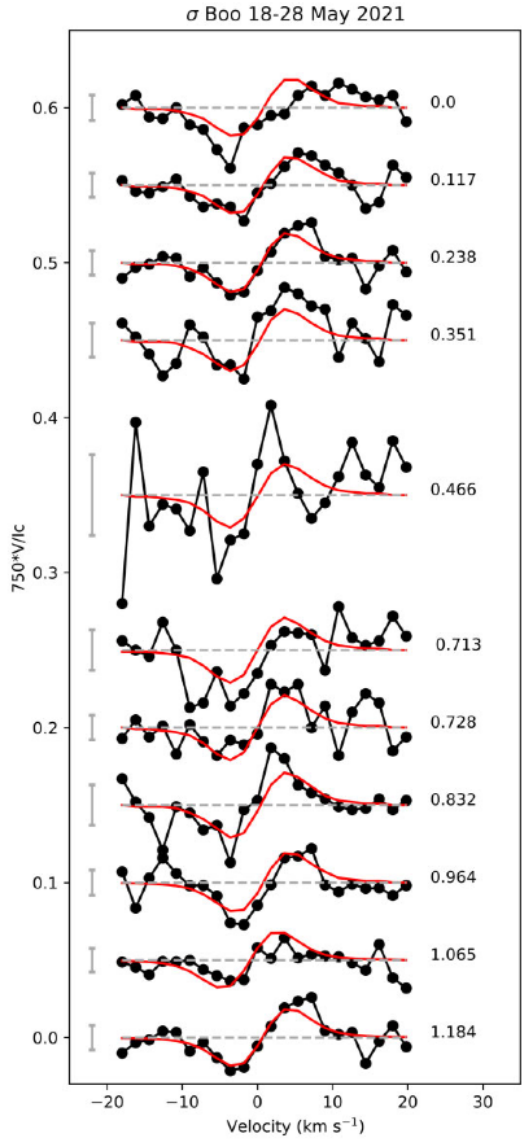

Figure 8. Stokes *V* fit for σ Boo corresponding to the 2021 magnetic maps. The description is the same as Fig. 7.

correlated with rotation rate (Balona & Abedigamba 2016), and with β CrB being a slow rotator ($v \sin i = 9.4$ km s^{-1}), we may therefore expect small or no detectable dΩ.

The presence of dΩ is a common feature of solar-type stars (Hall 1972; Gilman 1980; Rüdiger 1989) and is one of the ingredients in the operation of a solar-type dynamo (Parker 1955; Steenbeck & Krause 1969; Gilman 1980). We determine the amplitude of dΩ by applying a solar-type differential rotation law as described in Donati et al. (2000) where equatorial regions have larger angular velocity than polar regions:

$$\Omega(l) = \Omega_{\rm eq} - {\rm d}\Omega \sin^2 l, \quad (5)$$

where l denotes the latitude, $\Omega_{\rm eq}$ is the rotation rate at the equator, and dΩ is the rotational shear between the equator and the pole expressed in rad d^{-1}. The presence of dΩ in F-type stars was initially questioned by Gray (1982) who failed to find evidence of it in seven stars from F2-F8 using a Fourier transform of the line profiles. However, using a Fourier transform method, Reiners & Schmitt (2003a) detected dΩ was present in F-type stars. Further research has shown that strong dΩ may be present in F-type stars compared to cooler stars (Reiners & Schmitt 2003b; Barnes et al. 2005).

We do not find evidence of dΩ in σ Boo using the method of χ^2 minimization as described in Section 4.2.2. Reiners & Schmitt (2003a) found large dΩ values in comparably slowly rotating stars, therefore we may have expected σ Boo with a $v \sin i = 3.8$ km s^{-1} to have a high dΩ. Higher rates of dΩ are also expected to be present in earlier spectral types (Barnes et al. 2005). There are several possible reasons we did not find differential rotation in σ Boo. First, the magnetic field in σ Boo may have been too weak to allow magnetic features to be tracked on the surface of the star. A second reason is that rigid rotation may exist for σ Boo, therefore no dΩ was present in the star. A third reason for the lack of detection of dΩ may be due to a change in atmospheric conditions in early F-type stars whereby dΩ is inhibited near the transition to A-type stars (Walter 1983; Ammler-von Eiff & Reiners 2012). A fourth reason may be due to the presence of a varying differential rotation rate caused by a variable stellar dynamo (Marsden, Carter & Donati 2005), and σ Boo may have been observed during a period of low dΩ. The most likely reason for the non-detection of dΩ is the low amplitude of the Stokes *V* signal relative to the noise, and observations spanning only 1.2 rotation cycles.

5 CHROMOSPHERIC ACTIVITY INDICATOR

The *S*-index introduced by Vaughan, Preston & Wilson (1978) is an indirect measure of stellar magnetic activity in cool stars. It measures the flux in 20 Å wide triangular profiles centred on two resonance lines at 393.3682 nm (K-line) and 396.8492 nm (H-line) compared to the flux in two bands in the continuum on the red and blue side of the H&K line. The onset of chromospheric emission appears abruptly in solar-type stars (Hall 2008), and has been detected in the hot star Altair, A7 IV-V (Ferrero et al. 1995). Observations using the Far Ultraviolet Spectroscopic Explorer have suggested that chromospheres appear in stars as hot as 8250 K (Simon et al. 2002); however, the chromospheric emission is only a few per cent of the solar value. We do not determine *S*-index for β CrB since the measurement is not used in hot stars due to the absence of significant chromospheres (Hall 2008).

We determine the *S*-index for σ Boo using the method of Vaughan et al. (1978) and coefficients for the ESPaDOnS spectropolarimeter taken from Marsden et al. (2014). The *S*-index values for σ Boo are shown in table 6. We plot the rotational modulation of the mean nightly *S*-index of σ Boo in Fig. 11. The mean nightly *S*-index values vary from 0.248 ± 0.010 to 0.262 ± 0.005 and possibly show small variations in strength over the 11 d observation period. The figure indicates there is no periodic rotational modulation of the *S*-index. We confirm the lack of sinusoidal fit to the *S*-index data by applying a GLS periodogram to the mean *S*-index values and noted an absence of a detectable period to the 0.1 FAP level (see Fig. A1). Chromospheric emission dominates the flux measured in the *S*-index of K-type stars. However, Wolff, Heasley & Varsik (1985) suggest in active early F-type stars it is a minor contributor to the *S*-index. Variability in chromospheric emission may be difficult to detect in F-stars due to possible weakness of chromospheric emission and low contrast relative to the photospheric flux (Baliunas et al. 1995; Knutson, Howard & Isaacson 2010).

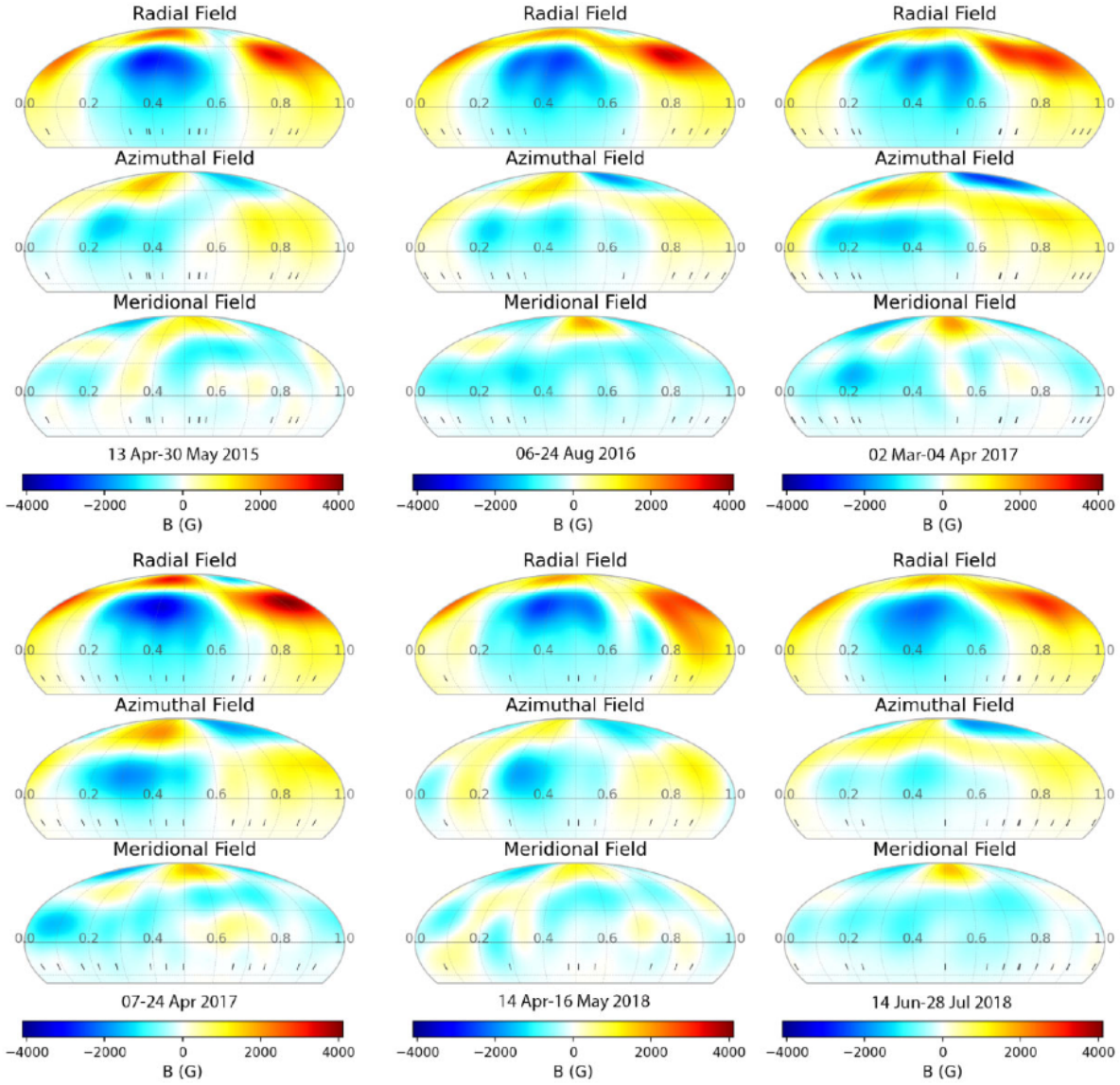

Figure 9. Magnetic maps for β CrB at six epochs from 2015–2018 displayed using a Mollweide projection. The magnetic field strength in gauss is indicated in colour bars below the maps. The radial, azimuthal, and meridional components of the reconstructed large-scale magnetic field are plotted from top to bottom. Tick marks at bottom of map indicate observational phases used in magnetic map reconstruction. The rotation phases for all maps are aligned to the same zero date of MJD = 2457126.47656 (2015 April 13). The map displays the visible surface of the star to −39 deg latitude.

6 DISCUSSION

6.1 β CrB

We have reconstructed for the first time surface magnetic maps for β CrB using ZDI. Our analysis of β CrB provides a rotational modulation of B_l that is consistent with previous studies. We find that the magnetic field is stable over the 4 yr observation period after taking into account the rotation of the magnetic field as a result of the different alignment in rotation and magnetic axes.

Using the simple oblique rotator model for β CrB, we find that our B_l max calculation of $+751.6 \pm 5.8$ G is 31.0 per cent of B_d value of 2423 ± 51 G, which is consistent with Schwarzschild's prediction that B_l should be about a third of the B_d value. Looking into the magnetic field in more detail beyond a simple dipole model, we find a range of maximum strengths of the magnetic field for the maps determined by ZDI from 2660 to 4106 G, which are larger than the B_l values of 902–1120 G. This may be due to some cancellation effects of the B_l where regions of opposite polarity cancel out, while less cancellation effects may occur in ZDI maps (Lehmann et al. 2019). A higher proportion of the magnetic energy is contained in higher multipoles, which is shown in our ZDI analysis that indicates for the six magnetic maps only 54–61 per cent of the magnetic energy is contained in the dipolar magnetic field, while a significant proportion of the energy is contained in the quadrupolar (18–20 per cent) and octupolar (5–8 per cent) components, and higher multipoles ($\ell >$ 3) account for 12–27 per cent of magnetic energy. This complex magnetic field for β CrB is also displayed in the magnetic maps that show details beyond a simple dipole. There are areas of positive and negative magnetic regions that are more commonly seen in dynamo fields.

Using arguments from Donati et al. (2006b), there are several reasons we conclude the complex magnetic field of β CrB is fossil in origin and not a dynamo field. First, β CrB is a relative slow rotator

Table 5. Fraction of the large-scale magnetic energy reconstructed in the toroidal and poloidal field components; the fraction of the poloidal field in the dipolar ($\ell = 1$), quadrupolar ($\ell = 2$), and octupolar ($\ell = 3$) components; and the fraction of the energy stored in the axisymmetric component ($m = 0$) for β CrB and σ Boo. The uncertainties are derived by varying the stellar parameters over the 1σ errors for each individual parameter, and taking the extreme values of the results as the variation.

Epoch (UT)	$B_{\rm mean}$ (G)	$B_{\rm max}$ (G)	Poloidal (per cent tot)	Toroidal (per cent tot)	Dipolar (per cent pol)	Quad. (per cent pol)	Oct. (per cent pol)	($\ell > 3$) (per cent pol)	Axisym. (per cent tot)	Poloidal (per cent axi)	Toroidal (per cent axi)
β CrB											
13 Apr–30 May 2015	970^{+44}_{-24}	3462^{+147}_{-87}	88^{+1}_{-1}	12^{+1}_{-1}	54^{+2}_{-2}	18^{+2}_{-1}	5^{+1}_{-0}	23^{+2}_{-2}	9^{+2}_{-2}	10^{+2}_{-2}	3^{+0}_{-0}
6–24 Aug 2016	1050^{+0}_{-104}	3624^{+0}_{-249}	89^{+0}_{-2}	11^{+2}_{-0}	57^{+0}_{-5}	19^{+0}_{-2}	7^{+0}_{-2}	17^{+7}_{-0}	23^{+0}_{-14}	23^{+0}_{-15}	20^{+0}_{-17}
2 Mar–4 Apr 2017	1113^{+0}_{-167}	3666^{+0}_{-179}	73^{+16}_{-0}	27^{+0}_{-16}	55^{+0}_{-3}	20^{+0}_{-3}	7^{+0}_{-2}	18^{+7}_{-0}	19^{+0}_{-12}	17^{+0}_{-9}	26^{+0}_{-23}
7–24 Apr 2017	1192^{+0}_{-246}	4106^{+0}_{-731}	85^{+4}_{-0}	15^{+0}_{-4}	50^{+5}_{-0}	18^{+3}_{-1}	5^{+1}_{-0}	27^{+0}_{-5}	13^{+0}_{-6}	14^{+0}_{-6}	11^{+0}_{-7}
14 Apr–16 May 2018	902^{+112}_{-0}	2660^{+949}_{-0}	90^{+0}_{-3}	10^{+3}_{-0}	54^{+1}_{-2}	20^{+0}_{-3}	8^{+0}_{-3}	18^{+7}_{-0}	7^{+4}_{-0}	7^{+5}_{-0}	7^{+0}_{-4}
14 Jun–28 Jul 2018	905^{+109}_{-0}	2906^{+703}_{-0}	87^{+2}_{-0}	12^{+0}_{-2}	61^{+0}_{-9}	21^{+0}_{-4}	6^{+0}_{-1}	12^{+13}_{-0}	21^{+0}_{-14}	20^{+0}_{-12}	30^{+0}_{-27}
σ Boo											
18–27 May 2021	$0.5^{+0.0}_{-0.0}$	$1.5^{+0.0}_{-0.0}$	95^{+1}_{-2}	5^{+2}_{-1}	84^{+1}_{-1}	14^{+1}_{-1}	2^{+0}_{-0}	2^{+1}_{-2}	88^{+2}_{-2}	92^{+2}_{-2}	10^{+5}_{-4}

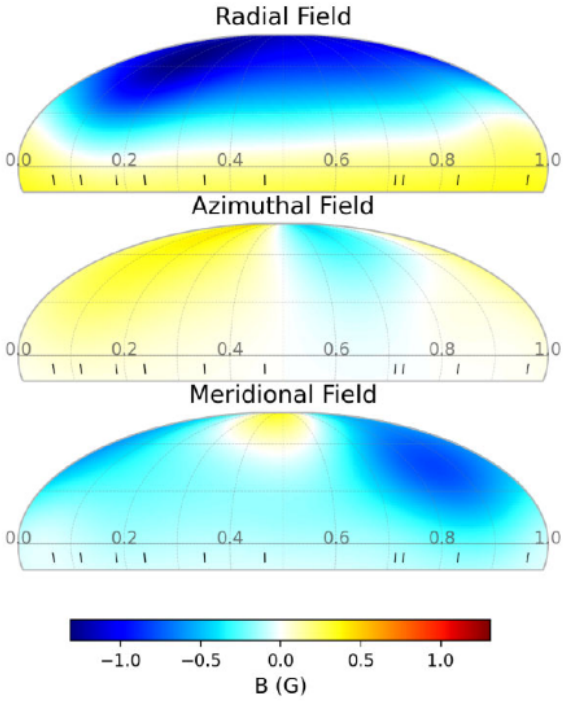

Figure 10. Magnetic map for σ Boo in 2021 reconstructed from mean LSD profiles. Description is the same as Fig. 9. Zero phase for the map is set to the first date of observations HJD = 2459352.82771. The map displays the visible surface of the star to −15 deg latitude.

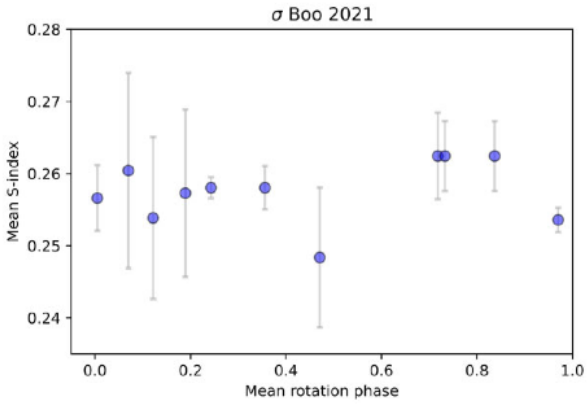

Figure 11. Rotational modulation of 11 mean nightly S-index values for σ Boo in 2021 May. The two closely spaced values at rotational phases 0.72 and 0.73 are observation on the same night separated by 2 h. The figure shows a small variation in S-index over time, but no variation due to rotational modulation.

($v \sin i = 9.4 \pm 0.2$ km s^{-1}) and dynamo-generated magnetic fields are expected to scale with rotation rate (Noyes et al. 1984). The $v \sin i$ is not fast enough to produce a large dynamo magnetic field of the order of several kG in strength. Secondly, we consider the possibility that the field is created by a convective core dynamo (Charbonneau & MacGregor 2001; Brun, Browning & Toomre 2005) that has reached the surface. According to Spruit–Taylor dynamo processes (Spruit 1999, 2002), a core dynamo would only be expected to reach surface strengths of a few gauss in a star rotating as slowly as β CrB. Thirdly, the large-scale magnetic field is stable over at least 3 yr, which contrasts with dynamo fields that are expected to evolve over time.

In order to maintain their stability, stellar fossil fields are thought to contain mixed poloidal and toroidal topology of comparable strength in their interior (Prendergast 1956; Tayler 1973; Wright 1973; Braithwaite & Spruit 2004; Braithwaite & Nordlund 2006). However, at the surface, they are expected to be mainly poloidal (Braithwaite 2009). We find that the surface magnetic field of β CrB is mainly poloidal (approximately 85 per cent) with 15 per cent being toroidal. This agrees with the expectation for a hot star fossil field. We also find that the magnetic field geometry of β CrB is not represented by a simple dipole as described by the oblique rotator model, but is more complex as suggested by Preston (1969), Wolff & Wolff (1970), Mathys & Hubrig (1997), and Bagnulo et al. (2000).

Complex fossil fields are rare, but have been found in several stars previously. τ Sco (B0.2 V) was found by Donati et al. (2006b) to contain an unusually complex surface magnetic field for a massive star that differed significantly from a simple dipole. The magnetic field contained a moderate toroidal component, which is unusual for a fossil field. The B_l varied over the rotation cycle from a minimum of -51.9 ± 5.3 G to a maximum of 87.8 ± 4.2 G. HD 37776 (B2IV) was found to show a complex, non-axisymmetric magnetic

field that differed from a simple dipole (Kochukhov et al. 2011). A quadrupolar component dominated the magnetic field geometry with higher multipoles present up to $\ell = 6$. The magnetic field intensity varied over the surface from ≈5 to ≈30 kG. The authors found that there were similar poloidal and toroidal components to the field, which was an unexpected result for a hot star that is not expected to contain such a high toroidal component.

The δ Scuti star HD 41641 (A5III) was found to contain a complex fossil field (Thomson-Paressant et al. 2021) B_l that varied from -178 ± 112 to 182 ± 273 G, and a simple dipole or dipole + quadrupolar configuration did not fit the data. Our finding of a relatively complex surface magnetic field for β CrB is at odds with the fossil field hypothesis where a complex magnetic field topology has previously been considered to be produced mostly by dynamo fields. Our results for β CrB are consistent with the presence of a complex fossil field and may add to the evidence that complex fossil fields may be more common than previously thought. Another δ Scuti star β Cas (F2III) has recently been shown to be magnetic (Zwintz et al. 2020); however, this time the complex magnetic field was considered to be produced by a dynamo. β Cas is therefore an interesting star for the study of magnetic fields in stars with shallow outer convection zones close to the transition between fossil and dynamo magnetic fields.

6.2 σ Boo

We have reconstructed surface magnetic maps for σ Boo at one epoch in 2021 May using ZDI. The surface magnetic topology is simple in structure, axisymmetric, poloidal (95 per cent), and is dominated by the dipole component (84 per cent) of magnetic energy. Less than 4 per cent of magnetic energy is contained in the higher ($\ell > 2$) multipoles. The simple magnetic field for σ Boo is similar to the late F-star β Vir F9V (Paper 2) and is more like the dipolar fields seen in hot stars. Complex surface topology does not appear to be a common feature of F-star dynamo magnetic fields, and may possibly be due to the shallow outer convection zones, which do not allow for complex twisting of the flux tubes on their rise to the surface.

σ Boo shows a variation of S-index over time, which is not due to rotational modulation. This is possibly due to magnetic areas on the surface of the star varying over time which may indicate a dynamo magnetic field. However, we are not able to definitely say whether the magnetic field of σ Boo is a dynamo field or weak fossil from a single epoch magnetic map. One or more additional epochs are required to characterize the field of σ Boo, and evolution of the large-scale magnetic field will indicate a dynamo field, while an unchanging field over an additional epoch will indicate that a weak fossil field in present.

The spectral type where the transition from fossil to dynamo magnetic fields occurs has not been determined; however, Paper 1 provided some evidence that it may occur as early as spectral type F3. This identifies σ Boo as an important star for magnetic studies. There is some indirect evidence that the F2IV star HD164615 may contain spots (Abt, Bollinger & Burke 1983; Zerbi et al. 1997), and therefore may be generated by a dynamo; however, this was questioned by Hatzes (1998) who concluded that the most likely explanation was non-radial pulsations.

Searching for dynamo magnetic field in stars earlier than F3 will help identify the transition between fossil and dynamo fields. Observing σ Boo at additional epochs will help firmly establish the nature of its magnetic field. Our mapping of a complex fossil field in β CrB and a simple dynamo field in σ Boo adds evidence that magnetic field complexity alone cannot be used to differentiate between fossil and dynamo fields. We need to look at a combination of factors in stars to fully categorize the type of surface magnetic field present. This includes B_l modelling, magnetic mapping, and chromospheric emission analysis.

7 CONCLUSIONS

Using ZDI, we reconstructed surface magnetic maps for β CrB (A9SrEuCr), a hot star with a fossil magnetic field, and σ Boo, an F3V star with either a dynamo field or a weak fossil field. The surface magnetic field of β CrB shows a relatively complex topology that is not commonly seen in hot stars with a fossil field. This adds further evidence that complex fossil fields might be more common than previously recognized. We also reconstruct surface magnetic maps for σ Boo and find that it has a relatively simple surface magnetic field topology. Future studies to search for dynamo magnetic fields in stars earlier than F3 will be valuable in order to learn more about the transition between fossil and dynamo magnetic fields.

ACKNOWLEDGEMENTS

This research was based on observations obtained at the Canada–France–Hawaii Telescope (CFHT), which is operated by the National Research Council of Canada, the Institut National des Sciences de l'Univers of the Centre National de la Recherche Scientifique of France, and the University of Hawaii. This work is based on observations obtained at the Bernard Lyot Telescope (TBL, Pic du Midi, France) of the Midi-Pyrénées Observatory, which is operated by the Institut National des Sciences de l'Univers of the Centre National de la Recherche Scientifique of France. This research was supported by an Australian Government Research Training Program (RTP). This research has made use of the SIMBAD data base, operated at CDS, Strasbourg, France, and the VizieR catalogue access tool, CDS, Strasbourg, France.

DATA AVAILABILITY

All data presented here are publicly available through the PolarBase data base (http://polarbase.irap.omp.eu/).

REFERENCES

Abramowitz M., Stegun A., 1964, Handbook of Mathematical Functions, 9th edn. Dover Press, New York
Abt H., Bollinger G., Burke E.,, Jr, 1983, ApJ, 272, 196
Adelman S. J., 1973, ApJ, 183, 95
Alfven H., Alfvén H., Fälthammar C., 1963, Cosmical Electrodynamics: Fundamental Principles, Clarendon Press, London
Ammler-von Eiff M., Reiners A., 2012, A&A, 542, A116
Aurière M., 2003, in Magnetism and Activity of the Sun and Stars, EDP Sciences, France, p. 105
Babcock H., 1947, ApJ, 105, 105
Babcock H., 1949, The Observatory, 69, 191
Babcock H. W., 1958, ApJS, 3, 141
Babcock H. W., 1960, ApJ, 132, 521
Bagnulo S., Landolfi M., Mathys G., Landi Degl'Innocenti M., 2000, A&A, 358, 929
Bagnulo S., Degl'Innocenti M. L., Landolfi M., Mathys G., 2002, A&A, 394, 1023
Baliunas S. A. et al., 1995, ApJ, 438, 269
Balona L. A., Abedigamba O. P., 2016, MNRAS, 461, 497
Baluev R. V., 2008, MNRAS, 385, 1279

Barnes J., Cameron A. C., Donati J.-F., James D., Marsden S., Petit P., 2005, MNRAS, 357, L1
Berdyugina S. V., 2005, Living Rev. Sol. Phys., 2, 8
Blazère A., Petit P., Neiner C., Folsom C., Kochukhov O., Mathis S., Deal M., Landstreet J., 2020, MNRAS, 492, 5794
Bothmer V., Daglis I., 2007, Space Weather: Physics and Effects, Springer Praxis Books. Springer-Verlag, Berlin
Braithwaite J., 2009, MNRAS, 397, 763
Braithwaite J., Nordlund Å., 2006, A&A, 450, 1077
Braithwaite J., Spruit H. C., 2004, Nature, 431, 819
Brandenburg A., Subramanian K., 2005, Phys. Rep., 417, 1
Brown E. et al., 2021, MNRAS, 501, 3981
Brun A. S., Browning M. K., Toomre J., 2005, ApJ, 629, 461
Bruntt H. et al., 2010, A&A, 512, A55
Burnette A. B., Canfield R. C., Pevtsov A. A., 2004, ApJ, 606, 565
Casagrande L., Schönrich R., Asplund M., Cassisi S., Ramírez I., Melendez J., Bensby T., Feltzing S., 2011, A&A, 530, A138
Charbonneau P., MacGregor K. B., 2001, ApJ, 559, 1094
Cowling T., 1945, MNRAS, 105, 166
Cowling T., 1957, Magnetohydrodynamics, Interscience Tracts on Physics and Astronomy. Interscience Publishers, London
Deutsch A. J., 1958, in Lehnert B., ed., Electromagnetic Phenomena in Cosmical Physics, Cambridge University Press, Cambridge, p. 209
Deutsch A. J., 1970, ApJ, 159, 985
Donati J.-F., Brown S., 1997, A&A, 326, 1135
Donati J.-F., Semel M., Rees D., 1992, A&A, 265, 669
Donati J.-F., Semel M., Carter B. D., Rees D., Cameron A. C., 1997, MNRAS, 291, 658
Donati J.-F., Mengel M., Carter B., Marsden S., Collier Cameron A., Wichmann R., 2000, MNRAS, 316, 699
Donati J.-F., Catala C., Landstreet J., Petit P., 2006a, in Casini R., Lites B. W., eds, ASP Conf. Ser. Vol. 358, Solar Polarization 4. Astron. Soc. Pac., San Francisco, p. 362
Donati J.-F. et al., 2006b, MNRAS, 370, 629
Donati J.-F. et al., 2008, MNRAS, 385, 1179
Dudorov A. E., Khaibrakhmanov S. A., 2015, Adv. Space Res., 55, 843
Falk A. E., Wehlau W. H., 1974, ApJ, 192, 409
Fares R. et al., 2009, MNRAS, 398, 1383
Fares R. et al., 2012, MNRAS, 423, 1006
Ferrero R. F., Gouttebroze P., Catalano S., Marilli E., Bruhweiler F., Kondo Y., Van Der Hucht K., Talavera A., 1995, ApJ, 439, 1011
Folsom C. P. et al., 2016, MNRAS, 457, 580
Folsom C. et al., 2018, MNRAS, 474, 4956
Fossati L. et al., 2015, A&A, 582, A45
Gaia collaboration, 2018, A&A, 616, A1
Gilman P. A., 1980, Differential Rotation in Stars with Convection Zones. Springer-Verlag, Berlin, p. 19
Glagolevskij Y., , 2003, in Piskunov N.et al. eds, Proc. IAU Symp. Modelling of Stellar Atmospheres. Cambridge University Press, Cambridge, UK, p. A3
Godolt M., Tosi N., Stracke B., Grenfell J. L., Ruedas T., Spohn T., Rauer H., 2019, A&A, 625, A12
Gray D., 1982, ApJ, 258, 201
Gray D., 2005, The Observation and Analysis of Stellar Photospheres. Cambridge Univ. Press, Cambridge
Grunhut J. et al., 2016, MNRAS, 465, 2432
Hall D. S., 1972, PASP, 84, 323
Hall J. C., 2008, Living Rev. Sol. Phys., 5, 1
Hanslmeier A., 2007, The Sun and Space Weather, Astrophysics and Space Science Library. Springer, Netherlands
Hatzes A., 1998, MNRAS, 299, 403
Järvinen S. et al., 2015, A&A, 574, A25
Jeffers S. et al., 2018, MNRAS, 479, 5266
Johnson H., Morgan W., 1953, ApJ, 117, 313
Kaltenegger L., Lin Z., 2021, ApJ, 909, L2
Knutson H. A., Howard A. W., Isaacson H., 2010, ApJ, 720, 1569
Kochukhov O., Lundin A., Romanyuk I., Kudryavtsev D., 2011, ApJ, 726, 24
Krause F., Radler K., 1980, Mean-field Magnetohydrodynamics and Dynamo Theory, Pergamon Press, Oxford, UK
Kurtz D., 1989, MNRAS, 238, 261
Lammer H., Khodachenko M., 2014, Characterizing Stellar and Exoplanetary Environments, Astrophysics and Space Science Library. Springer International Publishing, Switzerland
Landstreet J., Mathys G., 2000, A&A, 359, 213
Lehmann L., Hussain G., Jardine M., Mackay D., Vidotto A., 2019, MNRAS, 483, 5246
Leone F., Catanzaro G., 2001, A&A, 365, 118
Leroy J., 1995, A&AS, 114, 79
Lignières F., Petit P., Böhm T., Aurière M., 2009, A&A, 500, L41
Linsky J., 2019, Host Stars and their Effects on Exoplanet Atmospheres: An Introductory Overview, Lecture Notes in Physics. Springer International Publishing, Switzerland
Marsden S., Carter B., Donati J.-F., 2005, in Favata F.ed., 13th Cambridge Workshop on Cool Stars, Stellar Systems and the Sun. ESA, Noordwijk, Netherlands, p. 799
Marsden S. C., Mengel M. W., Donati F., Carter B. D., Semel M., Petit P., 2006, in Casini R.,Lites B., eds Solar Polarization 4. ASP, San Francisco, p. 401
Marsden S. et al., 2014, MNRAS, 444, 3517
Mason B. D., et al., 2001, AJ, 122, 3466
Mathis S., Zahn J.-P., 2005, A&A, 440, 653
Mathys G., 1989, Fundam. Cosm. Phys., 13, 143
Mathys G., 1993, in Dworetsky, M., Castelli, F.,Faraggiana R, eds, Peculiar versus normal phenomena in A-type and related stars. Cambridge University Press, Cambridge, UK, p. 232
Mathys G., 1995, A&A, 293, 733
Mathys G., Hubrig S., 1997, A&AS, 124, 475
Mestel L., 1966, MNRAS, 133, 265
Mestel L., 1967, in Magnetic and Related Stars. Mono Book Corporation, California, p. 101
Mestel L., 2012, Stellar Magnetism. Oxford Univ. Press, Oxford
Mestel L., Spitzer L., 1956, MNRAS, 116, 503
Moffatt H., 1978, Magnetic Field Generation in Electrically Conducting Fluids. Cambridge Univ. Press, Cambridge
Moffatt K., Dormy E., 2019, Self-Exciting Fluid Dynamos, Cambridge Texts in Applied Mathematics. Cambridge Univ. Press, Cambridge
Morin J., Donati J.-F., Petit P., Delfosse X., Forveille T., Jardine M., 2010, MNRAS, 407, 2269
Moss D., 2001, in Wickramasinghe D., et al., eds, Magnetic Fields Across the Hertzsprung-Russell Diagram. ASP, San Francisco, p. 305
Mullan D., 1972, ApL, 12, 13
Neiner C., Wade G., Sikora J., 2017, MNRAS, 468, L46
Noyes R., Hartmann L., Baliunas S., Duncan D., Vaughan A., 1984, ApJ, 279, 763
Oetken L., 1977, Astron. Nachr., 298, 197
Palubski I. Z., Shields A. L., Deitrick R., 2020, ApJ, 890, 30
Parker E. N., 1955, ApJ, 122, 293
Parker E., 1979, Cosmical Magnetic Fields: Their Origin and Their Activity. OUP, Oxford, UK
Parker E., 1987, Sol. Phys., 110, 11
Perryman M., 2018, The Exoplanet Handbook. Cambridge Univ. Press, Cambridge
Petit P., Donati J.-F., Collier Cameron A., 2002, MNRAS, 334, 374
Petit P. et al., 2008, MNRAS, 388, 80
Petit P. et al., 2010, A&A, 523, A41
Petit P., Louge T., Théado S., Paletou F., Manset N., Morin J., Marsden S., Jeffers S., 2014, PASP, 126, 469
Pettersen B., 1989, Sol. Phys., 121, 299
Pevtsov A. A., Canfield R. C., Metcalf T. R., 1994, ApJ, 425, L117
Piskunov N., Rice J., 1993, PASP, 105, 1415
Prendergast K. H., 1956, ApJ, 123, 498
Preston G., 1967a, in Cameron R., ed., Studies of Stellar Magnetism - Past, Present, and Future, in The Magnetic and Related Stars. Mono Book Corporation, California, p. 3
Preston G. W., 1967b, ApJ, 150, 547

Preston G. W., 1969, ApJ, 158, 1081
Preston G. W., Sturch C., 1967, in Magnetic and Related Stars. Mono Book Corporation, California, p. 111
Pyper D. M., 1969, ApJS, 18, 347
Reiners A., 2012, Living Rev. Sol. Phys., 9, 1
Reiners A., Schmitt J., 2003a, A&A, 398, 647
Reiners A., Schmitt J., 2003b, A&A, 412, 813
Renson P., Manfroid J., 2009, A&A, 498, 961
Roberts P. H., 1992, Dynamo Theory. Springer-Verlag, Berlin, p. 237
Rüdiger G., 1989, Differential Rotation and Stellar Convection: Sun and Solar-type Stars, Fluid Mechanics of Astrophysics and Geophysics. Gordon and Breach Science Publishers, New York
Rushby A. J., Shields A. L., Joshi M., 2019, ApJ, 887, 29
Ryabchikova T., Piskunov N., Kurucz R., Stempels H., Heiter U., Pakhomov Y., Barklem P. S., 2015, Phys. Scr., 90, 054005
Samus N., Kazarovets E., Durlevich O., Kireeva N., Pastukhova E., 2017, Astron. Rep., 61, 80
Schatzman E., 1962, Ann. Astrophys., 25, 18
Schmitt J., Golub L., Harnden F. Jr, Maxson C., Rosner R., Vaiana G., 1985, ApJ, 290, 307
Schneider F. R., Ohlmann S. T., Podsiadlowski P., Röpke F. K., Balbus S. A., Pakmor R., Springel V., 2019, Nature, 574, 211
Schwarzschild M., 1950, ApJ, 112, 222
Schwieterman E. W., Reinhard C. T., Olson S. L., Ozaki K., Harman C. E., Hong P. K., Lyons T. W., 2019, ApJ, 874, 9
Seach J., Marsden S., Carter B., Neiner C., Folsom C., Mengel M., Oksala M., Buysschaert B., 2020, MNRAS, 494, 5682 (Paper 1)
Seach J., Marsden S., Carter B., Evensberget D., Folsom C., Neiner C., Mengel M., 2022, MNRAS, 509, 5117 (Paper 2)
Segura A., Krelove K., Kasting J. F., Sommerlatt D., Meadows V., Crisp D., Cohen M., Mlawer E., 2003, Astrobiology, 3, 689
Semel M., 1989, A&A, 225, 456
Sikora J., Wade G., Power J., Neiner C., 2019, MNRAS, 483, 2300
Simon T., Ayres T. R., Redfield S., Linsky J. L., 2002, ApJ, 579, 800
Singh A. K., Bhargawa A., Siingh D., Singh R. P., 2021, Geosciences, 11, 286
Spitzer L., 1958, in Lehnert B., ed, Electromagnetic Phenomena in Cosmical Physics. Cambridge University Press, London, p. 169
Spruit H., 1999, A&A, 349, 189
Spruit H., 2002, A&A, 381, 923
Steenbeck M., Krause F., 1969, Astron. Nachr., 291, 49
Steinitz R., 1967, in Cameron R., ed., The Magnetic Oblique Rotator, in The Magnetic and Related Stars. Mono Book Corporation, California, p. 83
Stibbs D., 1950, MNRAS, 110, 395
Stift M., 1975, MNRAS, 172, 133
Strassmeier K. G., 2009, A&AR, 17, 251
Tayler R., 1973, MNRAS, 161, 365
Thomson-Paressant K., Neiner C., Zwintz K., Escorza A., 2021, MNRAS, 500, 1992
VanderPlas J. T., 2018, ApJS, 236, 16
Vaughan A. H., Preston G. W., Wilson O. C., 1978, PASP, 90, 267
Wade G., Donati J.-F., Landstreet J., Shorlin S., 2000, MNRAS, 313, 851
Walter F., 1983, ApJ, 274, 794
Walter F., Schrijver C., 1987, in Araki H., et al., eds, Cool Stars, Stellar Systems, and the Sun. Springer, London, p. 262
Wolff S. C., Wolff R. J., 1970, ApJ, 160, 1049
Wolff S. C., Heasley J., Varsik J., 1985, PASP, 97, 707
Wolff S. C., Boesgaard A. M., Simon T., 1986, ApJ, 310, 360
Wright G., 1973, MNRAS, 162, 339
Zahn J.-P., 2010, in Neiner C., et al. eds, Active OB stars: structure, evolution, mass loss, and critical limits, Cambridge University Press, Cambridge, UK, p. 14
Zechmeister M., Kürster M., 2009, A&A, 496, 577
Zeldovich I. B., Ruzmaikin A. A., Sokolov D. D., 1983, Magnetic Fields in Astrophysics. Gordon & Breach,, New York
Zerbi F. et al., 1997, MNRAS, 292, 43
Zwintz K. et al., 2020, A&A, 643, A110

APPENDIX A: ADDITIONAL DATA

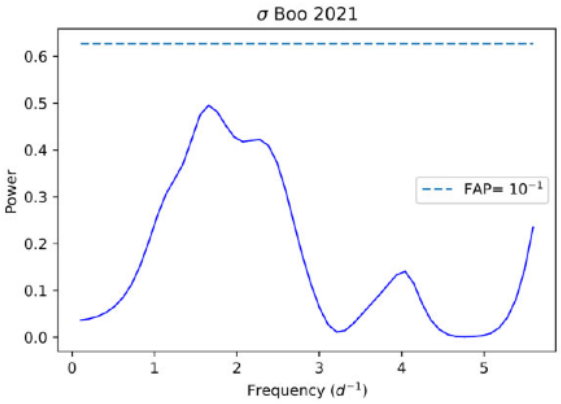

Figure A1. GLS periodogram a time-series of mean nightly *S*-index measurements for σ Boo spanning 11 d from 2021 May 18–28 (Table 2). The figure shows the power versus frequency and FAP, with no peak visible to the 10^{-1} level.

Table A1. Journal of observations for σ Boo in 2021 for the individual spectra. The columns are the same as Table 2.

Date (UT)	Time (UT)	Mid-HJD 2459000+	Rot. cycle	SNR Stokes I	RV (km s^{-1})	B_l (G)	N_l (G)	S-index	LSD lines used
May 18	06:46:45	352.78642	0.0000	714	0.29	−1.5 ± 1.5	−0.9 ± 1.5	0.257	17 654
May 18	06:57:27	352.79386	0.0009	715	0.29	−0.4 ± 0.5	0.0 ± 0.5	0.256	17 654
May 18	07:08:10	352.80130	0.0018	714	0.30	−3.0 ± 1.5	−0.7 ± 1.5	0.253	17 654
May 18	07:18:53	352.80874	0.0027	717	0.29	−0.6 ± 0.5	0.1 ± 0.5	0.262	17 654
May 18	07:29:36	352.81619	0.0035	717	0.28	−2.4 ± 1.4	−1.6 ± 1.4	0.256	17 654
May 18	07:40:20	352.82360	0.0044	714	0.29	−1.4 ± 0.5	0.4 ± 0.5	0.258	17 654
May 18	07:52:04	352.83179	0.0054	696	0.29	−3.5 ± 1.5	1.4 ± 1.5	0.247	17 654
May 18	08:02:47	352.83923	0.0063	713	0.31	−3.8 ± 1.2	−0.3 ± 1.2	0.262	17 654
May 18	08:13:30	352.84667	0.0072	711	0.30	−1.2 ± 0.8	0.5 ± 0.8	0.262	17 654
May 18	08:24:13	352.85411	0.0081	715	0.30	−1.5 ± 0.6	0.0 ± 0.6	0.251	17 654
May 18	08:34:56	352.86155	0.0089	715	0.30	−1.2 ± 0.5	0.4 ± 0.6	0.255	17 654
May 18	08:45:39	352.86900	0.0098	711	0.30	−1.3 ± 0.8	1.2 ± 0.8	0.260	17 654
May 19	06:18:56	353.76710	0.1167	719	0.32	−3.1 ± 1.4	0.3 ± 1.4	0.251	17 653
May 19	06:29:40	353.77455	0.1176	723	0.32	−2.2 ± 0.6	0.3 ± 0.6	0.263	17 652
May 19	06:40:24	353.78200	0.1185	722	0.32	−1.6 ± 0.5	0.8 ± 0.5	0.258	17 652
May 19	06:51:08	353.78946	0.1194	726	0.33	−1.0 ± 0.8	−0.6 ± 0.8	0.255	17 652
May 19	07:01:52	353.79691	0.1203	731	0.33	−1.6 ± 0.5	0.4 ± 0.5	0.259	17 652
May 19	07:12:37	353.80437	0.1212	731	0.34	0.7 ± 0.7	−0.5 ± 0.7	0.253	17 653
May 19	07:24:12	353.81242	0.1221	731	0.34	0.6 ± 0.5	0.6 ± 0.5	0.255	17 652
May 19	07:35:00	353.81992	0.1230	731	0.33	−0.6 ± 0.5	0.1 ± 0.5	0.261	17 652
May 19	07:45:47	353.82741	0.1240	733	0.34	1.3 ± 1.0	0.4 ± 1.0	0.254	17 652
May 19	07:56:31	353.83487	0.1248	729	0.34	−2.5 ± 1.3	0.5 ± 1.3	0.257	17 652
May 19	08:07:15	353.84232	0.1257	728	0.36	−0.8 ± 1.5	0.0 ± 0.5	0.261	17 652
May 19	08:18:04	353.84982	0.1266	711	0.36	−1.1 ± 0.5	0.1 ± 0.5	0.218	17 652
May 20	06:46:28	354.78620	0.2381	731	0.35	−1.5 ± 0.9	0.0 ± 0.9	0.256	17 653
May 20	06:57:13	354.79367	0.2390	724	0.35	−0.5 ± 0.6	0.5 ± 0.6	0.256	17 653
May 20	07:07:57	354.80112	0.2398	726	0.34	2.4 ± 1.6	−1.4 ± 1.6	0.257	17 652
May 20	07:18:43	354.80860	0.2407	724	0.34	−1.4 ± 1.0	0.5 ± 1.0	0.258	17 652
May 20	07:29:26	354.81604	0.2416	727	0.35	−1.1 ± 0.7	0.0 ± 0.7	0.257	17 653
May 20	07:40:12	354.82350	0.2425	732	0.34	−0.5 ± 0.5	−0.1 ± 0.5	0.258	17 653
May 20	07:51:43	354.83152	0.2435	728	0.35	−1.5 ± 0.6	−0.2 ± 0.6	0.259	17 653
May 20	08:02:27	354.83897	0.2444	722	0.34	−1.1 ± 0.6	−1.1 ± 0.6	0.257	17 652
May 20	08:13:10	354.84641	0.2452	730	0.33	−0.9 ± 0.7	0.0 ± 0.7	0.258	17 652
May 20	08:23:54	354.85386	0.2461	741	0.34	−1.2 ± 0.5	−0.1 ± 0.5	0.261	17 652
May 20	08:34:40	354.86134	0.2470	736	0.33	−0.9 ± 0.6	−1.3 ± 0.6	0.259	17 652
May 20	08:45:23	354.86878	0.2479	737	0.33	−2.1 ± 0.6	−0.8 ± 0.6	0.259	17 651
May 21	05:30:14	355.73325	0.3508	657	0.31	−3.0 ± 1.5	0.8 ± 1.5	0.249	17 651
May 21	05:41:00	355.74073	0.3517	655	0.31	−2.0 ± 0.8	−0.3 ± 0.8	0.249	17 651
May 21	05:51:44	355.74817	0.3526	658	0.31	−0.4 ± 0.6	−0.1 ± 0.6	0.254	17 651
May 21	06:02:27	355.75562	0.3535	653	0.30	−2.7 ± 1.6	−1.9 ± 1.6	0.255	17 652
May 21	06:13:10	355.76306	0.3544	646	0.31	2.2 ± 1.5	−1.6 ± 1.5	0.253	17 652
May 21	06:23:53	355.77051	0.3552	643	0.32	−2.8 ± 1.2	0.1 ± 1.2	0.256	17 652
May 21	06:35:59	355.77890	0.3562	576	0.33	−4.3 ± 2.6	0.1 ± 2.6	0.258	17 652
May 21	06:52:02	355.79005	0.3576	582	0.32	−3.6 ± 1.7	2.3 ± 1.7	0.255	17 652
May 21	07:02:45	355.79749	0.3585	608	0.32	−2.5 ± 0.9	0.9 ± 0.9	0.258	17 652
May 21	07:13:29	355.80494	0.3593	613	0.31	−1.5 ± 1.6	−0.5 ± 1.6	0.256	17 651
May 21	07:24:12	355.81239	0.3602	612	0.33	−4.5 ± 1.8	−0.9 ± 1.9	0.256	17 651
May 21	07:34:55	355.81983	0.3611	610	0.33	−3.6 ± 3.3	−3.4 ± 3.3	0.253	17 652
May 22	05:31:52	356.73437	0.4700	610	0.38	−3.3 ± 2.2	−2.4 ± 2.3	0.255	17 652
May 22	05:42:36	356.74181	0.4709	622	0.36	−3.4 ± 1.8	0.9 ± 1.8	0.235	17 652
May 22	05:53:19	356.74926	0.4718	583	0.37	−2.2 ± 1.3	1.8 ± 1.3	0.256	17 652
May 24	07:03:08	358.79770	0.7156	618	0.35	−1.6 ± 0.9	−0.6 ± 0.9	0.260	17 650
May 24	07:13:52	358.80517	0.7165	659	0.35	−1.4 ± 0.6	−0.3 ± 0.6	0.274	17 650
May 24	07:24:36	358.81261	0.7174	671	0.34	−3.0 ± 1.2	1.1 ± 1.2	0.257	17 650
May 24	07:35:19	358.82006	0.7183	668	0.35	−1.2 ± 0.6	0.0 ± 0.6	0.262	17 650
May 24	07:46:02	358.82750	0.7192	666	0.35	−4.1 ± 0.6	−0.5 ± 1.6	0.264	17 650
May 24	07:56:46	358.83495	0.7201	660	0.35	−1.3 ± 0.6	−0.7 ± 0.6	0.256	17 650
May 24	10:06:47	358.92524	0.7308	671	0.35	1.4 ± 1.1	0.7 ± 1.1	0.253	17 651
May 24	10:17:31	358.93269	0.7317	671	0.34	−1.5 ± 0.9	0.6 ± 0.9	0.257	17 650
May 24	10:28:14	358.94013	0.7326	672	0.34	−1.2 ± 0.9	0.2 ± 0.9	0.252	17 650
May 24	10:38:57	358.94757	0.7335	673	0.34	−1.9 ± 1.1	−1.5 ± 1.1	0.267	17 650
May 24	10:49:40	358.95502	0.7344	661	0.36	−2.8 ± 1.4	0.3 ± 1.4	0.259	17 650

Table A1 – *continued*

Date (UT)	Time (UT)	Mid-HJD 2459000+	Rot. cycle	SNR Stokes *I*	RV (km s^{-1})	B_l (G)	N_l (G)	*S*-index	LSD lines used
May 24	11:00:23	358.96246	0.7352	671	0.36	0.2 ± 0.6	0.7 ± 0.6	0.260	17 650
May 25	07:04:24	359.79856	0.8348	657	0.34	1.4 ± 1.6	−1.4 ± 1.6	0.251	17 650
May 25	07:15:07	359.80601	0.8357	651	0.35	1.4 ± 1.7	0.3 ± 1.7	0.255	17 650
May 25	07:25:54	359.81349	0.8366	654	0.34	−1.4 ± 0.6	0.0 ± 0.6	0.255	17 650
May 25	07:36:38	359.82095	0.8374	659	0.34	−1.7 ± 1.3	−0.1 ± 1.3	0.245	17 650
May 25	07:47:21	359.82839	0.8383	659	0.35	−2.7 ± 1.0	−0.3 ± 1.0	0.254	17 650
May 25	07:58:08	359.83588	0.8392	658	0.36	1.7 ± 1.5	0.6 ± 1.5	0.261	17 650
May 26	09:15:13	360.88939	0.9646	671	0.30	1.6 ± 1.3	−0.1 ± 1.3	0.251	17 650
May 26	09:25:56	360.89683	0.9655	675	0.30	−1.1 ± 0.8	0.8 ± 0.8	0.251	17 650
May 26	09:36:39	360.90428	0.9664	673	0.31	0.9 ± 0.6	−0.2 ± 0.6	0.256	17 650
May 26	09:47:22	360.91171	0.9673	678	0.30	−0.5 ± 0.5	0.1 ± 0.5	0.254	17 650
May 26	09:58:00	360.91916	0.9682	681	0.30	−0.6 ± 0.6	0.0 ± 0.6	0.255	17 650
May 26	10:08:48	360.92660	0.9691	682	0.30	−1.8 ± 1.4	−0.8 ± 1.4	0.254	17 650
May 26	10:20:33	360.93475	0.9700	684	0.30	−0.6 ± 0.5	0.0 ± 0.5	0.254	17 649
May 26	10:31:16	360.94220	0.9709	687	0.31	1.0 ± 1.0	−0.3 ± 1.0	0.251	17 650
May 26	10:41:59	360.94965	0.9718	687	0.31	2.8 ± 1.4	−1.3 ± 1.4	0.255	17 650
May 26	10:52:43	360.95709	0.9727	679	0.32	−0.8 ± 0.5	0.6 ± 0.5	0.253	17 650
May 26	11:03:26	360.91916	0.9736	675	0.31	−2.6 ± 1.5	−0.1 ± 1.5	0.255	17 650
May 26	11:14:09	360.97198	0.9745	681	0.32	−1.3 ± 0.5	−0.5 ± 0.5	0.252	17 649
May 27	05:29:08	361.73236	1.0650	710	0.36	−1.7 ± 1.4	−1.1 ± 1.4	0.242	17 649
May 27	05:39:52	361.73982	1.0659	713	0.35	−0.6 ± 0.5	−0.6 ± 0.5	0.254	17 648
May 27	05:50:36	361.74727	1.0668	718	0.36	−0.6 ± 0.5	−0.4 ± 0.5	0.265	17 648
May 27	06:01:19	361.75471	1.0677	715	0.36	1.8 ± 1.3	−0.5 ± 1.3	0.256	17 648
May 27	06:12:02	361.76216	1.0685	713	0.37	−2.0 ± 1.3	−0.9 ± 1.4	0.294	17 648
May 27	06:22:45	361.76960	1.0694	720	0.35	−1.5 ± 1.0	0.0 ± 1.0	0.266	17 648
May 27	06:34:11	361.77753	1.0704	719	0.35	−1.6 ± 1.3	−0.9 ± 1.3	0.273	17 648
May 27	06:44:54	361.78498	1.0713	472	0.35	−0.5 ± 1.5	1.2 ± 1.5	0.401	17 648
May 27	06:55:37	361.79242	1.0721	719	0.37	−0.7 ± 0.6	−0.6 ± 0.6	0.259	17 648
May 27	07:06:24	361.79991	1.0730	718	0.36	−0.5 ± 0.5	0.0 ± 0.5	0.258	17 648
May 27	07:17:07	361.80736	1.0739	722	0.36	1.3 ± 1.3	0.2 ± 1.2	0.245	17 648
May 27	07:27:51	361.81481	1.0748	724	0.36	−2.1 ± 0.9	1.4 ± 0.9	0.254	17 648
May 28	05:32:29	362.73466	1.1843	704	0.32	−1.6 ± 1.2	−0.9 ± 1.2	0.258	17 649
May 28	05:43:12	362.74212	1.1852	684	0.32	−5.0 ± 1.6	−1.3 ± 1.6	0.289	17 649
May 28	05:53:56	362.74956	1.1861	701	0.32	−1.0 ± 0.5	−0.9 ± 0.5	0.255	17 650
May 28	06:04:40	362.75701	1.1870	704	0.32	1.2 ± 0.8	−0.2 ± 0.8	0.256	17 650
May 28	06:15:23	362.76446	1.1879	434	0.31	2.2 ± 1.0	−2.5 ± 1.0	NA	17 646
May 28	06:26:06	362.77190	1.1887	712	0.33	−1.5 ± 0.6	−0.5 ± 0.6	0.259	17 650
May 28	06:37:28	362.77979	1.1897	709	0.33	−1.7 ± 0.6	−0.5 ± 0.6	0.256	17 650
May 28	06:48:14	362.78728	1.1906	709	0.33	−0.8 ± 0.5	−0.3 ± 0.5	0.259	17 649
May 28	06:58:58	362.79473	1.1915	708	0.33	−0.2 ± 0.5	−0.4 ± 0.5	0.260	17 649
May 28	07:09:42	362.80218	1.1924	704	0.33	−1.2 ± 0.5	−0.1 ± 0.5	0.246	17 649
May 28	07:20:30	362.80968	1.1932	698	0.32	−0.8 ± 0.5	−0.2 ± 0.5	0.250	17 650
May 28	07:31:13	362.81712	1.1941	694	0.32	0.2 ± 0.5	−0.3 ± 0.5	0.241	17 650

This paper has been typeset from a TEX/LATEX file prepared by the author.